Life and Liesegang:
Outcrop-Scale Microbially Induced Diagenetic Structures and Geochemical Self-Organization Phenomena Produced by Oxidation of Reduced Iron

Richard M. Kettler,[1] David B. Loope,[1] Karrie A. Weber,[1,2] and Paul B. Niles[3]

Abstract

The Kanab Wonderstone is sandstone (Shinarump Member, Chinle Formation) that is cemented and stained with iron oxide. The iron-oxide cementation and staining in these rocks have been considered examples of the Liesegang phenomenon, but we will show that they comprise a microbially induced structure. The spacing of bands of iron-oxide stain follow the Jablczynski spacing law (wherein the spacing between bands of iron-oxide stain increases as one traverses a series of bands) characteristic of Liesegang. Bands of iron-oxide cement exhibit more variable spacing and exhibit a weak but significant correlation between band thickness and distance between bands of cement. The pore-filling cement contains morphotypes that are similar in size and habit to those exhibited by microaerophilic iron-oxidizing bacteria. Other disseminated iron-oxide mineralization occurs as rhombohedra interpreted to be pseudomorphs after siderite. We interpret the cement to be produced by microbially mediated oxidation of siderite (a typical early diagenetic mineral in fluvial sandstones). Iron-oxidizing bacteria colonized the redox interface between siderite-cemented sand and porous sandstone. Microbes oxidized aqueous Fe(II), generating acid that caused siderite dissolution. The iron-oxide cement is the *microbial* product of a geochemical drive for organization; whereas the iron-oxide stain is true Liesegang. Together, they comprise a distinctive microbially induced structure with high preservation potential. Key Words: Biosignatures—Iron oxides—Diagenesis—Iron-oxidizing bacteria—Shinarump. Astrobiology 15, 616–636.

1. Introduction

IN THIS PAPER, we will examine patterned iron-oxide cement (IOC; iron-oxide mineralization that occludes pore space) and iron-oxide stain (IOS; iron-oxide mineralization that coats mineral grains but does not occlude pore space) (*e.g.*, Fig. 1). Many rocks that are cemented and stained in this fashion have been considered previously to be products of an abiotic Liesegang phenomenon. We will show that these features are actually products of evolving fluid-rock-*microbe* systems in aquifers. These fluid-rock-microbe systems generate millimeter- to centimeter-thick bands of microbially precipitated IOC as well as finer, apparently abiotic Liesegang bands. Proper interpretation of these cements and stains is important because they represent outcrop-scale evidence of preexisting life and they can occur in a wide variety of rock types.

Ornate patterns of IOC and IOS in porous rocks, referred to here as wonderstone (Fig. 1), are widespread. Among the best-known examples are exposures of the Breathitt Sandstone (Middle Pennsylvanian, Kentucky, USA) (Fu *et al.*, 1994), the Sharon Sandstone (Early Pennsylvanian, Ohio, USA) (Wells *et al.*, 2003), the Hawkesbury Sandstone (Permian, New South Wales, Australia) (Hunt *et al.*, 1977), the Umm Ishrin Sandstone (lower Paleozoic, Jordan) (Seilacher, 2001), and ''wonderstone'' (Fig. 1) from the Shinarump Member of the Chinle Formation (Triassic, Utah and Arizona, USA) (Hintze, 1986; Kettler *et al.*, 2010). These features are not limited to sandstones; similar patterns of iron-oxide cementation and staining have

---

[1]Department of Earth and Atmospheric Sciences, University of Nebraska-Lincoln, Lincoln, Nebraska.
[2]School of Biological Sciences, University of Nebraska-Lincoln, Lincoln, Nebraska.
[3]Astromaterials Research and Exploration Science, National Aeronautics and Space Administration, Lyndon B. Johnson Space Center, Houston, Texas.
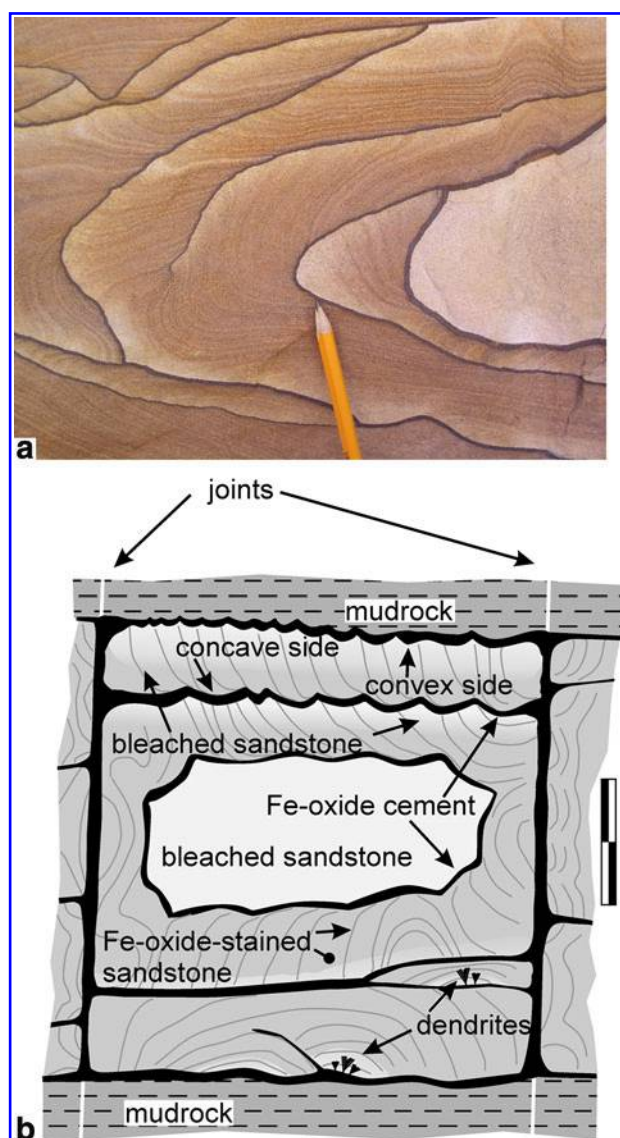
FIG. 1. Characteristics of wonderstone. (**a**) Image of wonderstone from the Shinarump Member of the Chinle Formation. Note pencil for scale. Dark red bands (as near pencil tip) are sandstone that has been cemented by iron oxide. The sandstone between layers of IOC has been variably stained with iron oxide. (**b**) Schematic diagram illustrating typical features of Shinarump wonderstone. Bar scale is 20 cm long. (Color graphics available at www .liebertonline.com/ast)

been described in Cretaceous carbonate rocks (Marko *et al.*, 2003; Serra *et al.*, 2010), Miocene andesite sills (Jamtveit *et al.*, 2011), and Cretaceous basalt (Singer and Navrot, 1970).

We have three reasons for studying the wonderstone phenomenon. (1) These features have long been considered to be enigmatic. The traditional explanation for these patterned rocks is that they are products of a geochemical self-organization process known as the Liesegang phenomenon (*e.g.*, L'Heureux, 2013, and references therein; Hintze, 1986; Fu *et al.*, 1994; Frankie and Jacobson, 2001; Seilacher, 2001; Marko *et al.*, 2003; McBride, 2003; Pickett,

2003; Serra *et al.*, 2010; Jamtveit *et al.*, 2011; Wells *et al.*, 2003; Wells *et al.* acknowledge but dispute the traditional Liesegang interpretation). Geochemical self-organization refers to the conversion of a geochemical system (*e.g.*, rock and aqueous solution; silicate melt) from ''an unpatterned to a patterned state without the intervention of an external template'' (Ortoleva *et al.*, 1987). Examples of geochemical self-organization include dissolution fingering at reaction fronts, oscillatory zoning in crystals, and orbicular granites (Ortoleva, 1994). The Liesegang phenomenon (Liesegang, 1896) is an example of chemical self-organization wherein bands of precipitate form in response to a migrating chemical front (*e.g.*, Feeney *et al.*, 1983; Antal *et al.*, 1998). The interpretation of these patterned rocks as products of the Liesegang phenomenon does not, however, address the source of chemical components, the timing of pattern formation, or the fluid chemistry responsible for mineral precipitation at specific localities. (2) Mineral cements are archives in which records of fluid-mineral interaction are stored, a fact that has prompted considerable interest in the origin of carbonate and silicate mineral cements (*e.g.*, Harwood *et al.*, 2013; Tomkinson *et al.*, 2013). IOCs have not, with recent exceptions (Chan *et al.*, 2012, and references therein; Weber *et al.*, 2012; Vasconcelos *et al.*, 2013; Reiners *et al.*, 2014), been subjected to the detailed study that is commonplace for carbonate or silicate cements. We are not aware, for example, of any attempts to test the Liesegang hypothesis of iron-oxide cementation in a specific formation. (3) The search for life on other planets has prompted an examination of lithological features that might be indicative of preexisting life. Ferric oxide minerals are highly insoluble and precipitate rapidly in oxidizing systems. They have been proposed as ideal recorders of ancient life and primary targets for sample return missions (Allen *et al.*, 2001). Hofmann and Farmer (2000) presented images of filamentous fabrics collected from a number of different terrestrial environments and proposed that evidence of microbial activity could be preserved in a wide variety of settings on other planets. Krepski *et al.* (2013) examined the morphology of a number of iron-oxidizing bacteria. They noted that a number of morphological characteristics associated with these microbes, taken collectively, were strong indicators of biogenicity and were, therefore, biosignatures. Weber *et al.* (2012) were able to link biosignatures to some unusual iron-oxide mineralization in the Navajo sandstone and proposed that a variety of unusual concretions were the product of microbial activity. Among the more successful attempts to find large-scale biosignatures has been the description of microbially induced sedimentary structures (MISS) (*e.g.*, Noffke, 2009). MISS are large (centimeter- to meter-scale) features produced by the interaction of microbial mats with unconsolidated sediment. The size of MISS allows them to be identified at the outcrop scale. MISS are, however, limited to sediments and sedimentary rocks by definition. MISS also can be vulnerable to erosion; many of the features form at the sediment surface and shallow subsurface. If the universe of microbially induced structures could be expanded to other rock types and to subsurface environments, exobiologists could greatly expand the range of rock types and past environments in which they might search for evidence of life profitably.
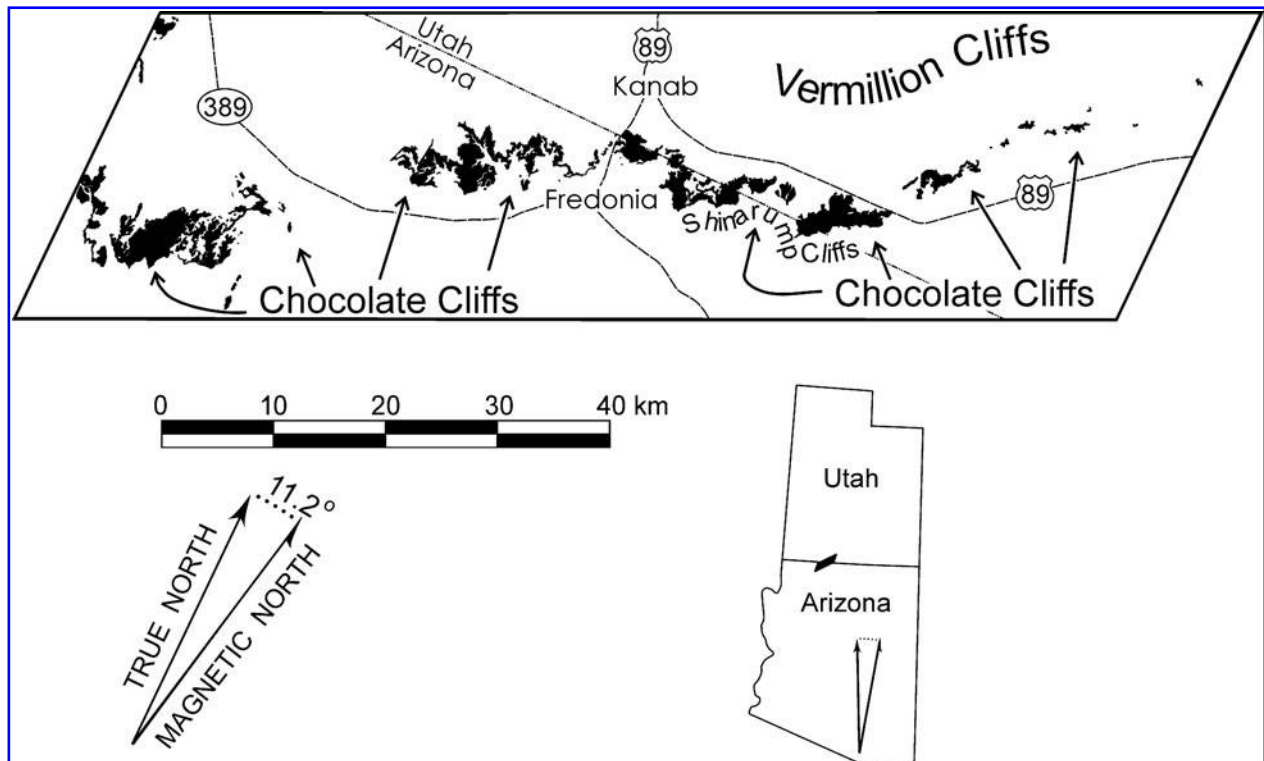
FIG. 2. Map of Shinarump Member exposures (black) in study area in southern Utah and northern Arizona. One portion of the Chocolate Cliffs east of Fredonia, Arizona, is referred to as the Shinarump Cliffs. Outcrop pattern after Billingsley *et al.* (2004, 2008), Sable and Hereford (2004), Hemphill (1956), and Morris (1957).
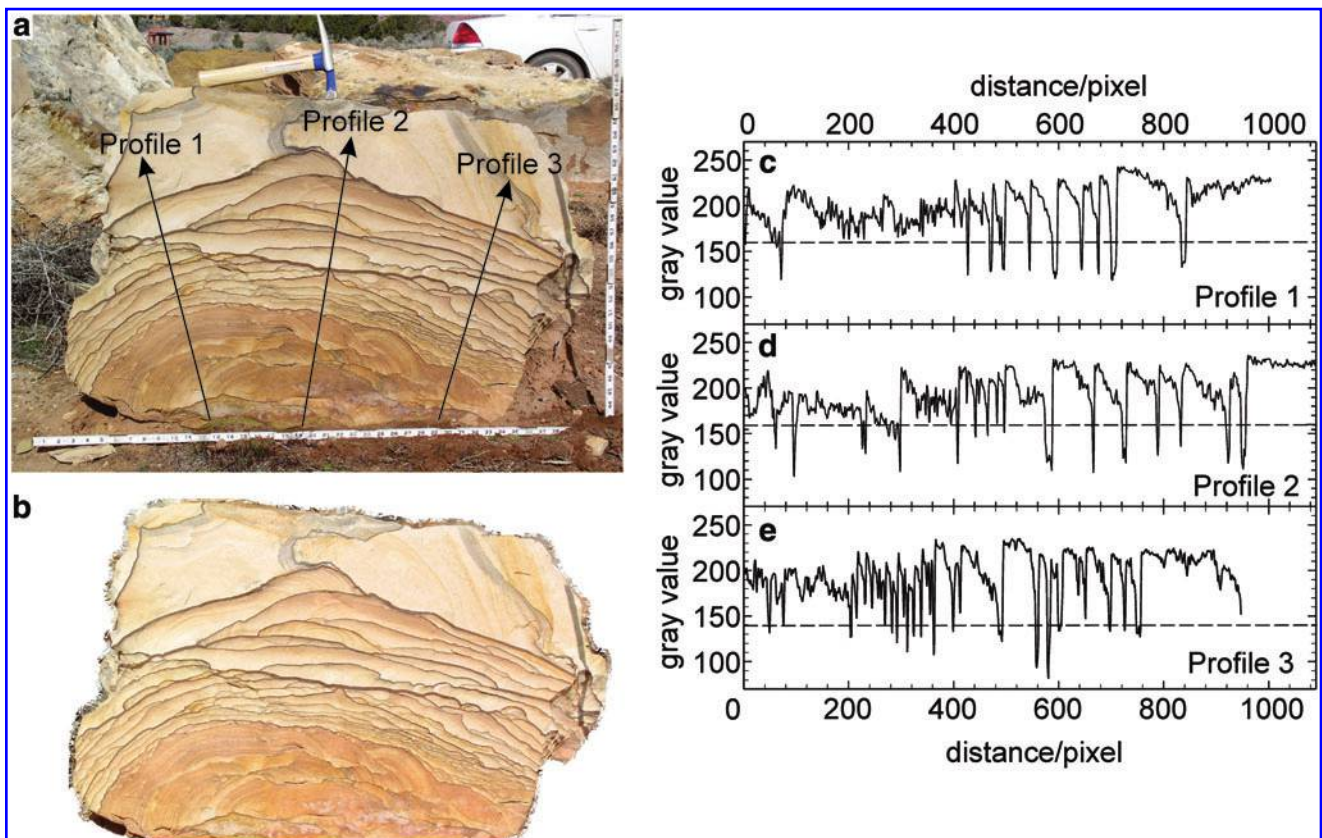

FIG. 3. Analysis of Image P3180044. (**a**) Image P3180044 of quarried block of Shinarump Member of Chinle Formation showing location of profiles. Note hammer and folding scale (English system) for reference. (**b**) Image shown in (a) after subtraction of background. (**c–e**) Gray value plotted as a function of pixel distance from origin for profiles 1–3, respectively. Dashed line is baseline gray value below which values are assigned to be cement. Scale is 20.3 pixel/cm. (Color graphics available at www.liebertonline.com/ast)

This paper focuses on the Kanab Wonderstone (or ''Picture Rock'') from the Shinarump Member of the Triassic Chinle Formation. We selected this material because it is sold widely as a decorative stone (Doelling and Davis, 1989); the sandstone coasters are a familiar sight at geol-ogy conventions, rock and mineral shows, and household goods retailers. We were, therefore, able to gain access to both quarried sites and large blocks of quarried Shinarump sandstone that provided fresh exposures of the iron-oxide mineralization. We will present evidence to support three
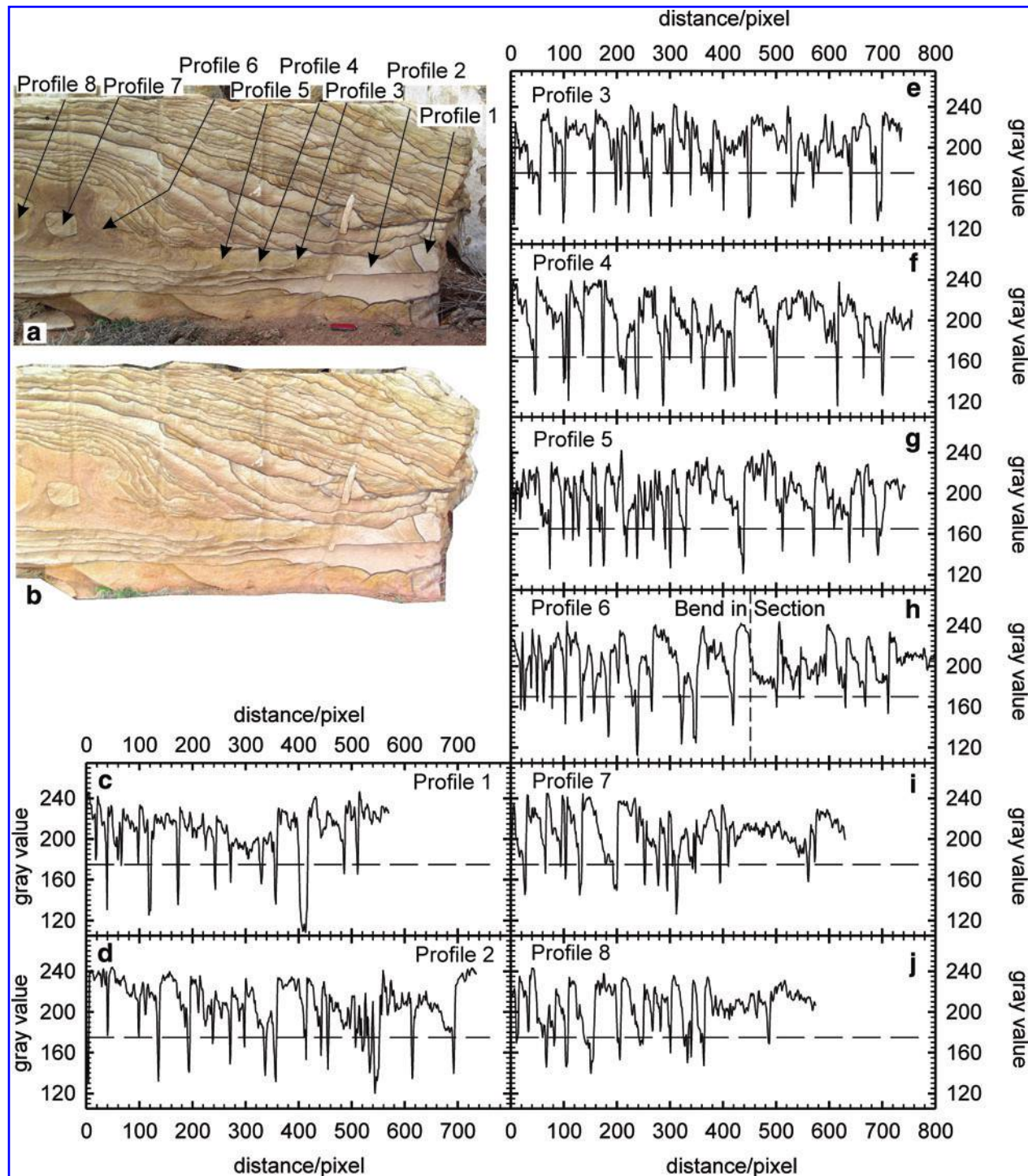

FIG. 4. Analysis of Image P3190192. (**a**) Image P3190192 of quarried block of Shinarump Member of Chinle Formation showing location of profiles. Note knife at bottom of image for scale. (**b**) Image shown in (a) after subtraction of background. (**c–j**) Gray value plotted as a function of pixel distance from origin for profiles 1–8, respectively. Dashed line is baseline gray value below which values are assigned to be cement. The bend in section in Profile 6 is shown by the vertical dashed line in (h). Scale is 12.4 pixel/cm. (Color graphics available at www.liebertonline.com/ast)

conclusions. (1) Wonderstone and similar-patterned IOC (iron-oxide mineralization that occludes pore space) and IOS (iron-oxide mineralization that coats mineral grains but does not occlude pore space) are products of evolving fluid-rock-*microbe* systems in aquifers. (2) A small amount of the iron oxide in the wonderstone pattern (the IOS) occurs as true Liesegang. This Liesegang forms as an integral part of the evolution of the fluid-rock-microbe system. (3) The Kanab Wonderstone can, therefore, be considered to comprise microbially induced structures. These microbially induced structures consist of thick bands of IOC precipitated as a consequence of microbial oxidation of iron and apparently abiotic Liesegang. They are similar to MISS in that they are centimeter- to meter-scale features interpreted to be evidence of preexisting microbial life but differ from MISS in that the mineral precipitates produced by the microorganisms are the distinctive features (*cf.* Noffke, 2009).

Those in search of extraterrestrial life must recognize that patterns in terrestrial rocks considered previously to be abiotic Liesegang include microbially mediated iron-oxide cementation. Moreover, when interpreted properly, these cements carry evidence of earlier diagenetic environments, directions of groundwater flow, and records of uplift and climatic conditions during uplift.

2. Geological Setting

The Shinarump Member of the Triassic Chinle Formation consists of conglomerates and sandstones that range from less than 1 m to 65 m in thickness (Hintze, 1986). The member is well known because it forms a resistant cap on the Moenkopi Formation in the Chocolate Cliffs of the Grand Staircase north of the Grand Canyon (Fig. 2) and the photogenic sandstone buttes and mesas of Monument Valley. It has also been explored extensively for uranium mineralization (Evensen, 1958). The detrital material that comprises the Shinarump was deposited in a northwest-flowing channel system that originated in the Grenville highlands in Texas (Dickinson *et al.*, 2010). The Shinarump is underlain by the non-marine siltstones and shales of the Moenkopi Formation and is overlain by Chinle Formation mudstones.

Wonderstone within the Shinarump Member (Fig. 1) consists of jointed blocks of sandstone that have been cemented and stained with iron oxide. The IOC (Fig. 1) occurs as bands as thick as 2 cm. The bands of IOC are undulatory and when viewed in detail comprise a series of cusps. We use the orientation of these cusps in combination with the orientation and distribution of the IOS to define convex and concave sides to the bands of IOC (Fig 1). The curved bands of IOS typically abut the convex side of the IOC and are asymptotic to the concave side of the IOC (Fig. 1). The convex sides of the IOC are notable for the occurrence of manganese oxide dendrites and sandstone bleaching, whereas sandstone abutting the concave side of the IOC is stained pervasively with iron oxide (Fig. 1). The sandstone bleaching may include apparent removal of IOS. The cores of some jointed blocks are completely enclosed by a single thick rind of IOC and bleached. Such bleached cores are noted only when the bands of IOC are convex toward the interior of the jointed block (Fig. 1).

3. Materials and Methods

Quarried blocks, exposures, and samples from a variety of locations in southern Utah and northern Arizona (Fig. 2) were examined. Fragments obtained by fracturing sandstone were cleaned with purified water and methanol and allowed to dry overnight at 314 K. The dried fragments were placed on a scanning electron microscope (SEM) stub, sputter-coated with a gold-palladium alloy, and stored in a desiccator. Samples were imaged on a Hitachi S4700 field-emission
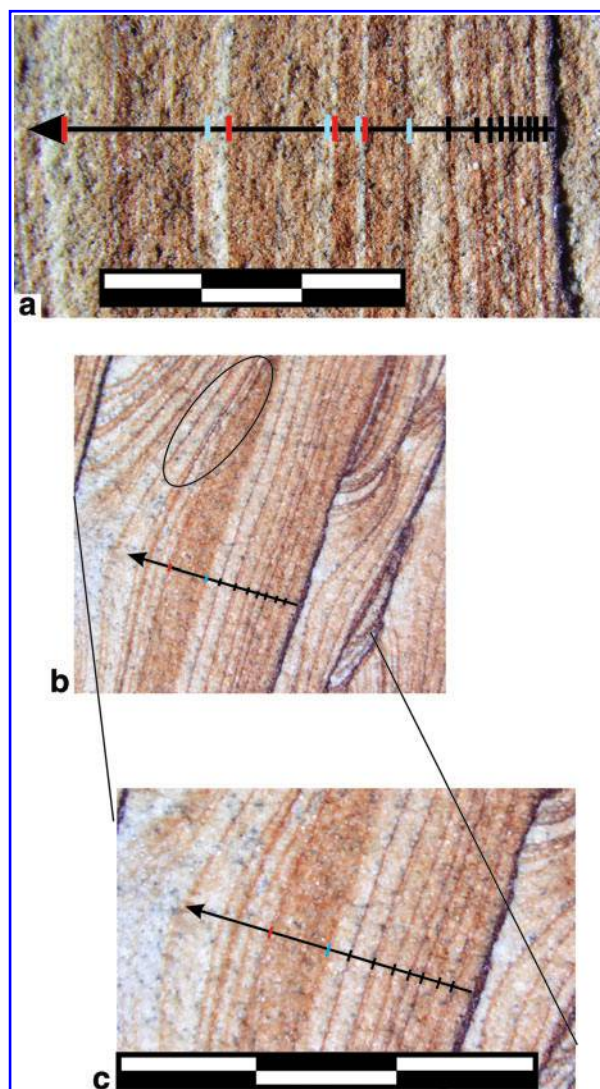

FIG. 5. (**a**) Image P8270107 of block of Shinarump Member of Chinle Formation showing profile and location of bands of IOS. Scale bar is 15 mm long. Black tick marks are placed at the center of bands of IOS, whereas blue and red tick marks denote the edges of a band of IOS. (**b**) Image P8260106 of block of Shinarump Member of Chinle Formation showing profile and location of bands of IOS. (**c**) Enlargement of area shown in (b). Scale bar is 15 mm long. Profile was terminated because of interference from another set of bands of IOS [see circled area in (b)]. Black tick marks are placed at the center of bands of IOS, whereas blue and red tick marks denote the edges of a band of IOS. (Color graphics available at www.liebertonline.com/ast)

Table 1. Results of Regression Analysis Testing Spacing Law for Images P3180044
Profiles 1–3 and P3190192 Profiles 1–8

	Profile		DoF[a]	SS[b]	MS[c]	T[d]
P3180044	1	Regression	1	684580	684580	−0.750
		Error	11	99873	9079	
		Total	12	784453		
	2	Regression	1	1165903	1165903	0.283
		Error	17	22276	1310	
		Total	18	1188179		
	3	Regression	1	784756	784756	−0.004
		Error	22	17734	806	
		Total	23	802490		
P3190192	1	Regression	1	234591	234591	0.674
		Error	9	3681	409	
		Total	10	238272		
	2	Regression	1	453780	453780	−1.336
		Error	16	9960	622	
		Total	17	463740		
	3	Regression	1	773984	773984	2.322
		Error	21	8045	383	
		Total	22	782029		
	4	Regression	1	579660	579660	1.415
		Error	15	12327	822	
		Total	16	591987		
	5	Regression	1	785451	785451	1.502
		Error	21	11080	528	
		Total	22	796531		
	6	Regression	1	878196	878196	2.972
		Error	18	7191	7191	
		Total	19	885387		
	7	Regression	1	298825	298825	0.719
		Error	12	18121	1510	
		Total	13	316846		
	8	Regression	1	221521	221521	0.242
		Error	12	12879	10732	
		Total	13	234400		

[a]Degrees of freedom.
[b]Sum of squares.
[c]Mean square.
[d]T statistic for H_0: slope $= 1$, H_1: slope > 1.

SEM at 5 and 10 kv at the Morrison Microscopy Core Research Facility at the University of Nebraska-Lincoln. Samples were also examined at 15 kV on the JEOL 5910LV SEM equipped with an energy-dispersive X-ray spectroscopy system at the Johnson Space Center.

Images of quarried blocks of the Shinarump Member (Figs. 3a and 4a) were processed using Image J software (Schneider *et al.*, 2012). A series of profiles were struck across each examined image. The profiles were oriented so that the pixel number increased in the "convex direction." Images were processed by subtracting background using the light background option and rolling ball radius algorithm with radius set to 50 pixels (Figs. 3b and 4b). It was these processed images over which the profiles (Fig. 3c–3e and Fig. 4c–4j) were collected. A threshold gray value was then set for each profile by inspection to distinguish bands of IOC from areas of sandstone stained with iron oxide.

The value of X_n is taken to be the distance from the beginning of the profile to the center of the nth band. The width of the nth peak (W_n) is defined as the number of pixels for which the gray value is less than the designated threshold (Fig. 3c–3e and Fig. 4c–4j).

Profiles through bands of IOS (Fig. 5) were oriented to be orthogonal to bands of IOC. The bands of IOS were identified by inspection and the distance (X_n) from the start of the profile to the middle of each band recorded.

The retrieved values of X_n and W_n were processed using least-squares linear regression. The analysis of variance

Table 2. Results of Regression Analysis Testing Spacing Law for Images P8260106 and P8270107[a]

Image	DoF	SS	MS	T[b]
P8260106				
Regression	1	109470	109470	3.550
Error	5	2318	464	
Total	6	111788		
P8270107				
Regression	1	2786886	2786886	9.282
Error	9	26834	2981	
Total	10	2813720		

[a]See Table 1 for explanation of column headings.
[b]H_0: slope $= 1$, H_1: slope > 1.

TABLE 3. RESULTS OF REGRESSION ANALYSIS TESTING RELATIONSHIP BETWEEN IOC BAND THICKNESS[a] AND DISTANCE BETWEEN BANDS FOR IMAGES P3180044 AND P3190192

	Profile		Concave			DoF	Convex		
			SS	MS	F[b]		SS	MS	F[b]
P3180044	1	Regression	0.037	0.037	0.0031	1	21.403	21.403	2.140
		Error	141.392	11.783		12	120.025	10.002	
		Total	141.429			13	141.428		
	2	Regression	0.032	0.032	0.0032	1	29.551	29.551	1.166
		Error	190.918	10.607		18	161.399	89.666	
		Total	190.950			19	190.950		
	3	Regression	8.968	8.968	1.405	1	41.687	41.687	8.405
		Error	146.792	6.382		23	114.073	4.960	
		Total	155.760			24	155.760		
	Stacked	Regression	3.812	3.812	0.430	1	88.105	88.105	11.946
		Error	504.696	8.854		57	420.404	7.376	
		Total	508.508			58	508.509		
P3190192	1	Regression	2.163	2.163	0.1022	1	81.541	81.541	6.171
		Error	211.504	21.150		10	132.126	13.213	
		Total	213.667			11	213.667		
	2	Regression	8.113	8.113	1.4625	1	12.083	12.083	2.2739
		Error	94.308	5.548		17	90.338	5.314	
		Total	102.421			18	102.421		
	3	Regression	26.337	26.337	3.3959	1	20.016	20.016	2.489
		Error	170.621	7.756		22	176.942	8.043	
		Total	196.958			23	196.958		
	4	Regression	3.189	3.189	0.7161	1	4.024	4.024	0.9143
		Error	71.255	4.453		16	70.420	4.041	
		Total	74.444			17	74.444		
	5	Regression	1.036	1.036	0.2491	1	19.184	19.184	5.757
		Error	91.464	4.157		22	73.315	3.332	
		Total	92.500			23	92.499		
	6	Regression	4.484	4.484	1.209	1	1.574	1.574	0.4076
		Error	70.468	3.709		19	73.378	3.862	
		Total	74.952			20	74.952		
	7	Regression	5.672	5.672	1.416	1	0.282	0.282	0.0646
		Error	60.093	4.006		15	65.483	4.366	
		Total	65.765			16	65.765		
	8	Regression	2.691	2.691	2.691	1	20.889	20.889	1.166
		Error	251.042	1.931		13	232.844	17.911	
		Total	253.733			14	253.733		
	Stacked	Regression	2.281	2.281	0.300	1	96.724	96.725	13.916
		Error	1123.113	7.756		148	1028.670	6.950	
		Total	1125.394			149	1125.394		

[a]See Table 1 for explanation of column headings.
[b]F statistic for H_0: slope $= 0$, H_1: slope > 0.

(ANOVA) tables derived from this exercise are presented in Tables 1–3. The column labeled DoF contains the number of degrees of freedom for the regression (1 independent variable), for the error (number of observations—2), and the total (the number of observations—2 + 1). The label SS designates the "sum of squares" and refers to the sum of squared deviations of the dependent variable about the mean (SS Total), the sum of squared deviations of each value held by the dependent variable from its predicted value given the value of the paired independent variable (sum of squares about the regression or residual sum of squares; SS Error), and the difference between SS Total and SS Error (sum of squares due to regression; SS Regression). The label MS designates "mean square" and is obtained by dividing each sum of squares value by the corresponding number of DoF.

The t statistic (see Eq. 1.4.4 of Draper and Smith, 1966) is designated by T, whereas the F statistic (Eq. 1.4.10 of Draper and Smith, 1966) is designated by F. Guides to interpretation of ANOVA tables generated by linear regression can be found in the work of Draper and Smith (1966) or comparable resources.

4. Results

4.1. Petrography

Examination with scanning electron microscopy revealed iron-oxide mineralization with a variety of habits. Pore-filling IOC comprises predominantly abundant plates with a crude hexagonal appearance that may be as large as $10\,\mu m$ in long dimension (Fig. 6a). Locally, the iron-oxide grains
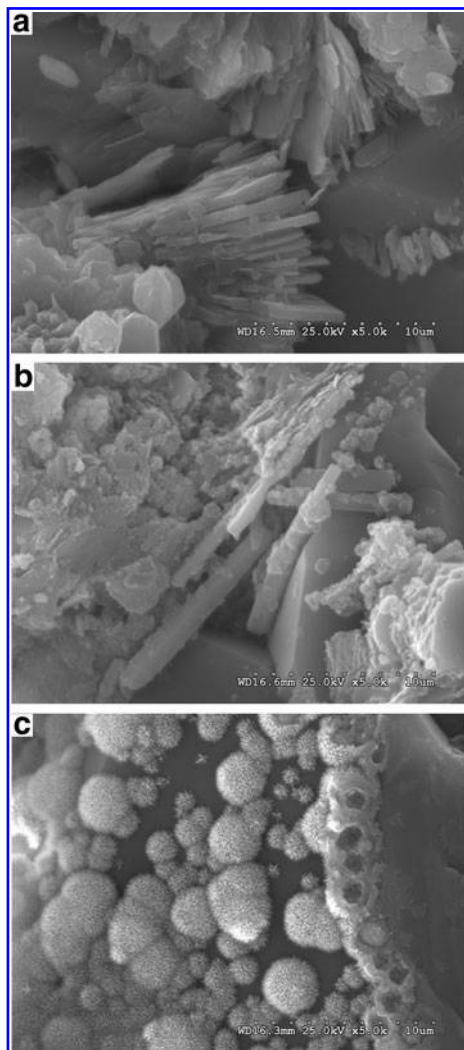
FIG. 6. (**a**) SEM image of numerous hexagonal plates of iron-oxide cement filling pore space between quartz sand grains. (**b**) SEM image of iron-oxide cement comprising hexagonal plates and lath-like mineral grain (in lower center of image). Note the late-stage clumps of acicular grains occurring as an overgrowth on all other forms of iron oxide. (**c**) SEM image of hemispherical aggregates of iron-oxide needles on a quartz grain.

have an acicular to lath-like habit and align to form platy aggregates (Fig. 6b). Spherical aggregates of iron-oxide needles comprise local discontinuous coatings on the surface of quartz grains and all other forms of iron-oxide mineralization (Fig. 6b–6c).

We also observed numerous twisted stalks and filaments (Fig. 7) near the edges of IOC. These stalks are as long as 200 μm and range from 0.7 to 2 μm in diameter. These filaments are locally overgrown with iron-oxide mineralization or trapped within the rock by quartz grains. They typically consist of 20 or fewer individual filaments that are twisted with helical angles ranging from 75° to 85° (Fig. 7c) and are ornamented locally with hexagonal plates. Some of the stalks branch on one end (Fig. 7d). Analysis of the stalks by wavelength-dispersive spectroscopy indicated that they consist of C, Fe, Si, and Al with local traces of Cu (Fig. 8).
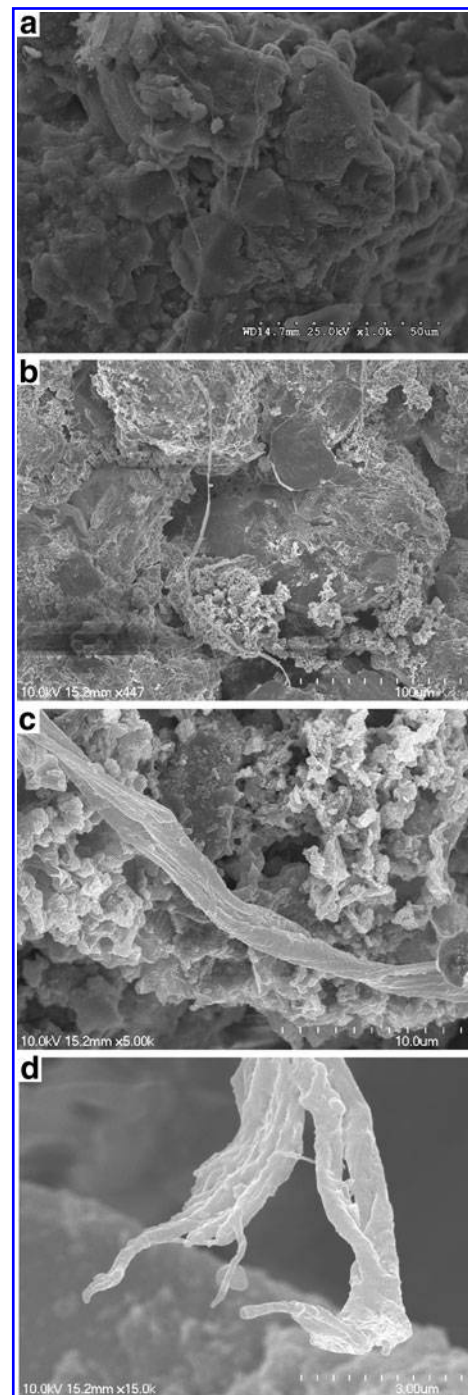

FIG. 7. (**a**) SEM image of numerous twisted filaments cemented to quartz grains and covered locally by IOC. (**b**) Image of long twisted filament anchored to iron-oxide cement at top of image. (**c**) Detailed SEM image of portion of feature shown in (b) illustrating the number of filaments in the stalk, the twisted nature of the stalk, and the relationship to IOC. (**d**) Detailed SEM image of the free end of stalk shown in (b) and (c).

In addition to the IOC and IOS, we also observe local disseminated iron-oxide mineralization in the Shinarump Member. Much of this disseminated mineralization comprises equant iron-oxide rhombohedra (Fig. 9) when viewed in thin section.
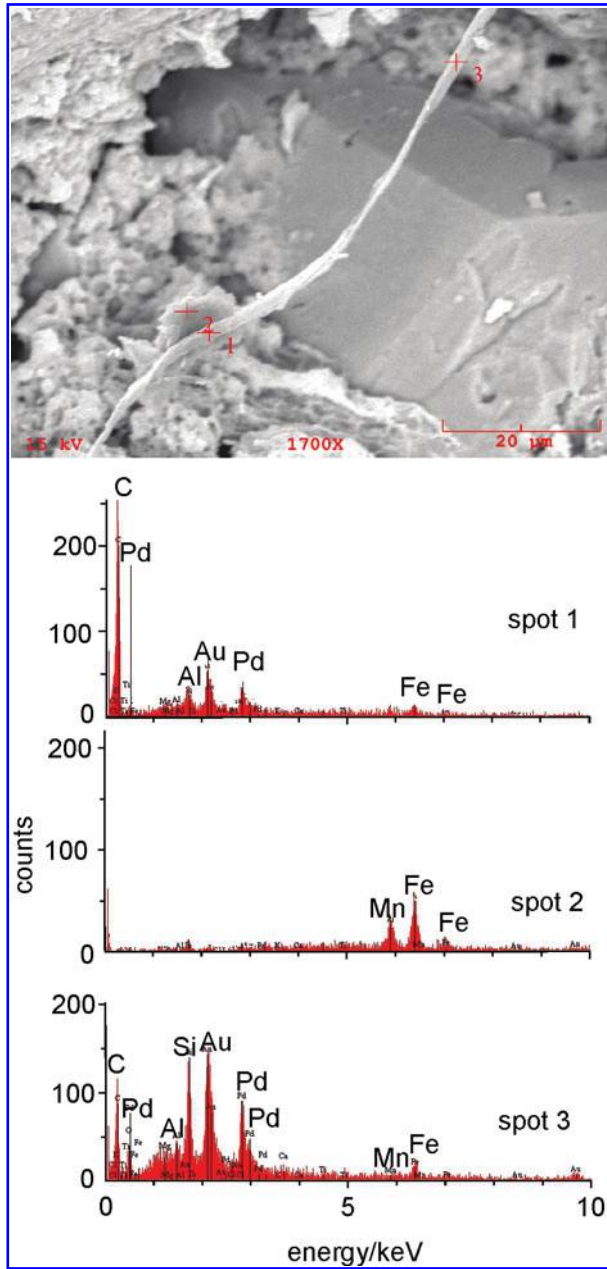
FIG. 8. SEM image of portion of stalk shown in Fig. 7b with the energy-dispersive spectra generated by analysis of the spots labeled in the SEM image. Bar scale is 20 μm long. Note large euhedral quartz grain for reference. Numbered crosses indicate positions of electron beam during analyses. Spectra are presented as generated by the instrument after redrafting the axes and relabeling some peaks for clarity. Spot 2 is located off the stalk and detects only Fe and Mn, whereas the analyses located on the stalk (Spots 1 and 3) detect Fe, Mn, C, Si, and Al. The Pd and Au response is from the conductive coating placed on the samples before analysis. (Color graphics available at www.liebertonline .com/ast)

4.2. Spatial analysis of IOC and IOS

Iron-oxide mineralization similar to wonderstone has traditionally been interpreted as a type of periodic precipitate, typically referred to as Liesegang banding. Liesegang bands are distinctive because the spacing of the bands of precipitate is neither random nor even. Band spacing may increase or decrease as the distance from the solution interface increases (Ortoleva, 1984, p 289). However, so-called revert spacing, wherein the distance between bands decreases systematically as distance from the solution interface increases, is rare (Karam *et al.*, 2011). The exact mechanism by which Liesegang bands form remains controversial (Henisch, 1988; Jamtveit and Hammer, 2012). For example, one model involves supersaturation of a pore fluid with the requisite mineral phase, followed by nucleation and growth of precipitate bands. Bands of precipitate then grow at the expense of potential nucleation sites on either side of the bands; solute is driven to the nucleation sites within bands by diffusion (*e.g.*, Antal *et al.*, 1998). In an alternative model, precipitate bands form as larger particles grow at the expense of smaller ones, dissolution and reprecipitation being driven by the lower surface free energy of the larger particles (*e.g.*, Feeney *et al.*, 1983). Experimental work has shown that nanoparticle precipitates will grow, re-dissolve, and form bands of coarser, re-deposited precipitate with the passage of time after two solutes have been introduced at a solution interface (Al-Ghoul *et al.*, 2012).

We use geometric and morphological features of the IOC and IOS to test whether the Liesegang model can be applied to wonderstone. The hypothesis that the entire collection of iron-oxide cementation and staining in wonderstone is the product of the Liesegang phenomenon can be dismissed readily. In particular, the discordant orientation of the bands of IOC and IOS (Fig. 1), the asymmetric distribution of bleached and stained rock, and orientation of these elements with respect to the convex and concave sides of each band of IOC require that cementation proceeded in a specific direction. We therefore tested the hypothesis that the IOC and IOS were separate Liesegang systems.

Liesegang bands typically obey a number of laws with respect to the spacing between bands, band width, and the timing of band formation (*e.g.*, Antal *et al.*, 1998). The spacing law (or Jablczynski law) (Jablczynski, 1923) states that the ratio of the distances of two consecutive bands from the solution interface is given by

$$X_n/(X_{n-1}) \rightarrow 1+p \qquad (1)$$

where X_n and X_{n-1} are the distance of the n and n - 1 bands, respectively, from the interface between the two solutions, and p is a constant between 0.05 and 0.4.

We performed this analysis on IOC in blocks of Shinarump wonderstone (Figs. 3 and 4). No single solution front can be assigned *a priori* to any series of IOC bands present within any block of Shinarump sandstone. On the other hand, the ratio defined in Eq. 1 should still converge to $1+p$ if the distance is measured from any arbitrary point in a direction approximately orthogonal to the IOC bands if they are true Liesegang. If the bands are spaced randomly, then the value of p approaches zero and indicates that the Liesegang phenomenon is not a likely explanation for the band geometry and spacing.

Regressions of X_n on X_{n-1} yield straight lines with slopes that approach 1 (Figs. 10 and 11). The ANOVA analyses of the regressions (Table 1) test the null hypothesis that the

FIG. 9. Photomicrograph of sample of sandstone from Shinarump Member. The large, light grains are quartz clasts, whereas the blue areas are pore space that has been filled with dyed epoxy. The reddish-brown rhombohedral grains in the center of the image are interpreted to be iron-oxide pseudomorphs after siderite. Image taken in plane-polarized light. (Color graphics available at www.liebertonline.com/ast)
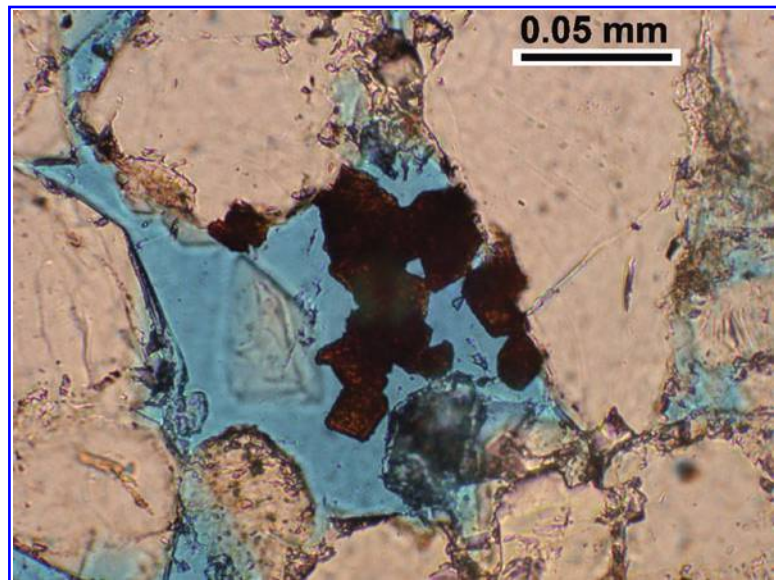
slope of each line is 1 against the alternative hypothesis that the slope is greater than 1. The null hypothesis cannot be rejected for any of the profiles (Fig. 10) obtained from Image P3180044 with an attained significance less than or equal to 0.05. The null hypothesis can be rejected for two (Profile 3 and Profile 6) of the eight profiles (Fig. 11) obtained from Image P3190192. The slopes of these two profiles are still very close to 1, indicating very small values for p. The value of p in Eq. 1 is, therefore, considered to be 0 for the bands of IOC in the wonderstone samples from the Shinarump Member. Because the distance between bands does not increase systematically in any direction, we conclude that the bands of IOC are not Liesegang.

In contrast to the IOC, coherent sets of IOS do follow the Jablczynski spacing law and are likely true Liesegang. Two examples of bands of IOS that parallel bands of IOC are shown in Fig. 5. The bands of IOC are taken as the origins for profiles orthogonal to the bands. The spacing law can be tested by measuring the distance from the midpoints of each of the bands to the origin. These results are used to test the spacing law in Fig. 12 with the results of the regression of X_n on X_{n-1} presented in Table 2. The T statistic presented in Table 2 is calculated for testing the null hypothesis that the slopes of the regression lines are 1 compared to an alternative hypothesis that the slopes are greater than 1. In both cases, the null hypothesis can be rejected in favor of the alternative hypothesis with an attained significance less than 0.01. The calculated slopes for the two regression lines are 1.3 and 1.44, values that are consistent (within assigned error) with the Jablczynski spacing law (Antal *et al.*, 1998).

4.3. Test of IOC band thickness versus distance between bands

Inspection of a number of blocks of wonderstone led us to conclude that the thicker bands of IOC were associated with larger intervals between bands of IOC. This relationship is only evident, however, if one moves across the block in the

direction in which the IOC bands are convex. We tested this relationship by regressing W_n against $X_n - X_{n-1}$, where W is the width of a particular band of IOC (Figs. 13 and 14). The null hypothesis that there is no relationship between band width and distance between bands cannot be rejected (with attained significance <0.05) when distance is measured in the concave direction (Table 3). On the other hand, when the analysis is performed in the convex direction (W_n regressed against $X_{n+1} - X_n$; Figs. 13 and 14), the null hypothesis can be rejected (with attained significance <0.05) for Profile 3 from Image P3180044 and Profiles 1 and 5 from Image P3190192. Each of the profiles from an individual block should examine the same set of IOC bands. The results, therefore, can be combined to minimize random error in a fashion similar to stacking of seismic data to increase signal-to-noise ratio (Robinson, 1985). After stacking the profiles for both images, the null hypothesis can be rejected with an attained significance less than 0.001 for both images (Table 3). Thus, there is a relationship between width of the IOC bands and distance between bands, but only when measured in the convex direction.

5. Discussion

Any interpretation of the wonderstone pattern must accommodate the five observations and conclusions as follows: (1) The bands of IOC are not Liesegang. (2) The thickness of any band of IOC is related to the distance to the next succeeding band of IOC, but only when proceeding in the convex direction. (3) The bands of IOC contain petrographic evidence of microbially mediated precipitation of iron oxide. (4) The bands of IOS are Liesegang. (5) One can find local patches of IOC consisting of rhombohedra that we interpret to be pseudomorphs after siderite.

Our interpretation of the Shinarump wonderstone is that the sandstone was cemented locally with siderite during early methanic diagenesis. The sandstone was fractured by joints during Basin and Range tectonism and infiltrated by oxygenated groundwaters during uplift of the Colorado Plateau. Iron-oxidizing bacteria colonized the redox
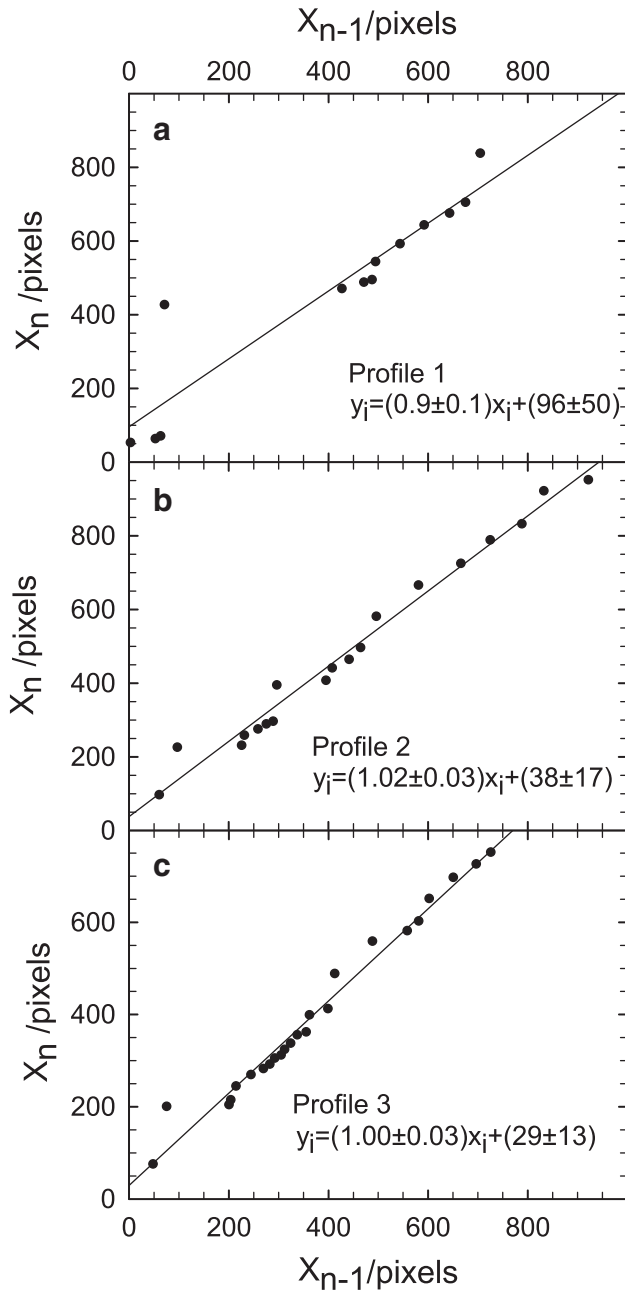
FIG. 10. (a–c) Results of tests of spacing law for profiles taken on Image P3180044 (Fig. 3), Profiles 1–3, respectively. All regressions of X_n on X_{n-1} yield slopes equal to unity.

interface between the oxidizing groundwaters and siderite cement. Aqueous Fe^{2+} that diffused to the stabilized redox interface was oxidized by the microbes and precipitated as iron oxide.

The insolubility of ferric hydroxides requires that iron be transported in aqueous solution either under reducing or strongly acidic conditions. We have found little evidence for strongly acidic conditions in the Shinarump. Although pyrite is ubiquitous in sedimentary systems, the depositional environment of the Shinarump is not favorable for deposition of abundant pyrite. The Shinarump is

a non-marine sandstone sandwiched between the continental red beds of the Moenkopi Formation below and those in other members of the Chinle Formation above. The sandstones contain little evidence of acid-sulfate weathering. Minerals such as jarosite or alunite are absent. Some pyrite remains preserved within the Shinarump and can be observed in outcrop to be oxidizing slowly. Cubic or pyritohedral iron oxides that might be produced by oxidation of pyrite are, however, rare. We propose that the iron accumulated locally in the Shinarump as siderite cement. The equant iron-oxide rhombohedra (Fig. 9) are direct evidence for the presence of siderite. Partially oxidized rhombohedral ("diamond-shaped") siderite grains have been observed in ancient rocks (Lai *et al.*, 2012), and siderite is a typical early diagenetic mineral in fluvial sandstones (Berner, 1981).

The interpretation that iron-oxide cementation proceeded in a specific direction was made based on the discordant orientation of the bands of IOC and IOS (Fig. 1) and the asymmetric distribution of bleached and stained rock relative to the IOC. This interpretation is confirmed by the relationship between IOC band width and distance between bands. This relationship is best explained if the iron that now resides in the bands of IOC was obtained from the region on the convex side of each band of IOC. We conclude, therefore, that the bands of IOC are not produced by solutes diffusing freely throughout the rock or the Ostwald ripening of nanoparticles distributed throughout the rock, but rather result from the oxidation of preexisting Fe-bearing minerals located only on the convex side of each band of IOC.

The iron-oxidizing bacterium *Gallionella* spp. "can be easily identified because of its distinctive stalk, which appears in the form of bundled fibers arranged in a double helix" (Hallberg and Ferris, 2004). Recent research supports that the distinctive helical stalk is a product of the physiology of microaerophilic iron-oxidizing bacteria and can be considered a biosignature for past iron-oxidizing metabolic activity (Krepski *et al.*, 2013), which can also be preserved in porous medium (Weber *et al.*, 2012). The morphology of the stalks and filaments observed here is identical to that described by Hallberg and Ferris (2004). The stalks have similar lengths, diameters, and numbers of filaments, and the filaments are twisted with similar helical angles. Although the individual filaments are slightly thicker than those observed in modern *Gallionella* spp., the aggregate diameter of the bundled filaments is comparable to that observed for both modern *Gallionella* spp. (Hallberg and Ferris, 2004) and documented examples of microfossils of Fe(II)-oxidizing organisms (Weber *et al.*, 2012; Krepski *et al.*, 2013). The branching shown in Fig. 7c and 7d is similar to that observed in stalks formed by Fe(II)-oxidizing bacteria. In those stalks, it is interpreted to result from cell division during stalk growth (Krepski *et al.*, 2013). The composition of the filaments is similar to that reported for samples of modern *Gallionella* spp. (Ridgway *et al.*, 1981; Kim *et al.*, 2002; Suzuki *et al.*, 2011). More importantly, carbon was detected only in the filaments; adjacent plates consist of only iron, manganese, and apparently oxygen (Fig. 8). The morphological and chemical evidence collectively comprise strong evidence that the filaments were produced biogenically.
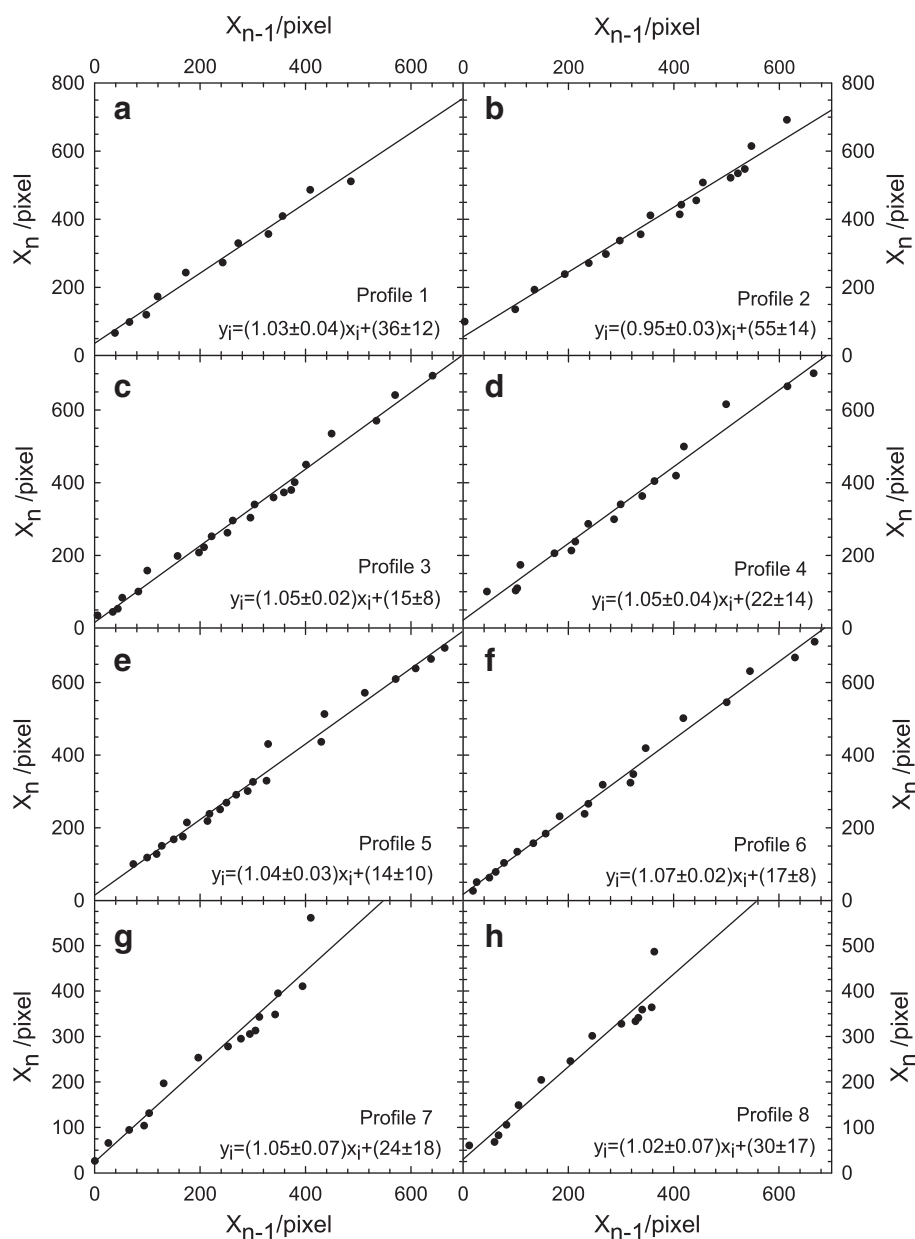
FIG. 11. (a–h) Results of tests of spacing law for profiles taken on Image P3190192 (Fig. 4), Profiles 1–8, respectively. All regressions of X_n on X_{n-1} yield slopes equal to or very close to unity.

Profile 1: $y_i = (1.03 \pm 0.04)x_i + (36 \pm 12)$

Profile 2: $y_i = (0.95 \pm 0.03)x_i + (55 \pm 14)$

Profile 3: $y_i = (1.05 \pm 0.02)x_i + (15 \pm 8)$

Profile 4: $y_i = (1.05 \pm 0.04)x_i + (22 \pm 14)$

Profile 5: $y_i = (1.04 \pm 0.03)x_i + (14 \pm 10)$

Profile 6: $y_i = (1.07 \pm 0.02)x_i + (17 \pm 8)$

Profile 7: $y_i = (1.05 \pm 0.07)x_i + (24 \pm 18)$

Profile 8: $y_i = (1.02 \pm 0.07)x_i + (30 \pm 17)$

The density and abundance of preserved filaments similar to modern *Gallionella* spp. (Fig. 7) are less than typically observed in modern seeps (*cf.* Fig. 2 of Emerson and Revsbech, 1994). The relatively low density of filaments may reflect the difference between a fossilized accumulation of iron oxide and a modern setting chosen because of the dense and abundant growth of iron-oxidizing bacteria. Even within a modern setting in which *Gallionella* stalks are abundant, such stalks are best observed on the top 1–2 mm of the mat. At greater depth within modern microbial mats, *Gallionella* stalks become progressively encrusted with particulate iron oxides (Emerson and Revsbech, 1994). We had greater success identifying twisted stalks on the periphery of the bands of IOC as opposed to the central portions of the bands. In these latter regions, pore space was filled completely with cement consisting largely of hexagonal plates

of iron oxide (Fig. 6a and 6b). Furthermore, community succession during iron oxidation could also comprise a transition from *Gallionella* spp. dominance to a community dominated by another iron-oxidizing microorganism (Fleming *et al.*, 2014). We have observed iron encrusted bacilli-like structures in IOCs previously (Weber *et al.*, 2012). Given the distinctive morphology and evidence for preservation of *Gallionella* and similar species (*e.g.*, Weber *et al.*, 2012; Krepski *et al.*, 2013), however, we focused on the twisted stalk morphology as a biosignature indicator for past metabolically active iron-oxidizing microbiota.

The composition, size, and overall morphology of the filaments illustrated in Fig. 7 are evidence that Fe(II)-oxidizing bacteria such as *Gallionella* spp. were present during oxidation of iron and precipitation of ferric oxyhydroxides. Iron-oxidizing bacteria are chemolithotrophs
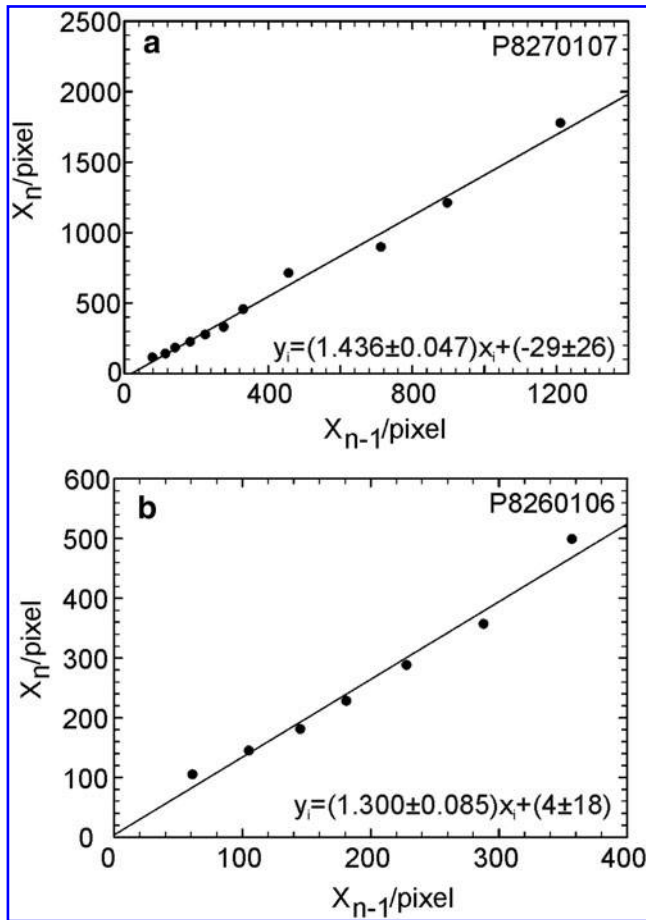
FIG. 12. (**a**) Results of test of spacing law for profile taken in Image P8270107 (shown in Fig. 5a) and (**b**) Image P8260106 (shown in Fig. 5b and 5c). Both profiles yield slopes greater than 1 with values that are consistent with the Jablczynski spacing law (Antal *et al.*, 1998). Scale for Image P8270107 is 60 pixel/mm, whereas scale for Image P8260106 is 75.2 pixel/mm.

that oxidize ferrous iron to ferric iron following the reaction

$$4Fe^{2+}_{(aq)} + xO_{2(aq)} + (1-x)CO_{2(aq)} + 4H^+_{(aq)}$$
$$= 4Fe^{3+}_{(aq)} + (1-x)CH_2O_{(am)} + (1+x)H_2O \quad (2)$$
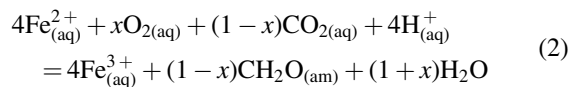
Whereas some microbes can utilize aqueous CO_2 as a carbon source (Hallberg and Ferris, 2004; Emerson *et al.*, 2010), *Gallionella* spp. can utilize $FeCO_3$ as a substrate and precipitate Fe^{3+} as ferric oxyhydroxide following the net reaction

$$4FeCO_3 + (1-x)O_{2(aq)} + 10H_2O$$
$$= 4Fe(OH)_3 + xCH_2O_{(am)} + (4-x)HCO^-_{3\ (aq)} + (4-x)H^+_{(aq)} \quad (3)$$
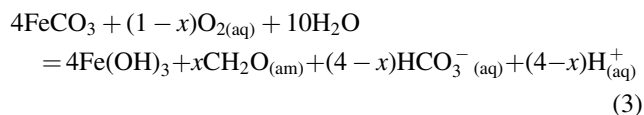
The production of acid during the latter reaction is important for three reasons, as follows: (1) Production of acid

in close proximity to the cell membrane has been proposed to increase the proton motive force and thus the energy-generating potential of the cell (Chan *et al.*, 2004). (2) Excess acid is neutralized by dissolution of siderite tending to drive the reaction from left to right. This mechanism of siderite oxidation is very similar to one we proposed for iron-oxide concretions in the Navajo and Dakota Sandstones (Loope *et al.*, 2010, 2011, 2012; Weber *et al.*, 2012). (3) The iron oxide that is latest paragenetically comprises spherical and hemispherical aggregates of iron-oxide needles (Fig. 6c). This *pin cushion* habit is characteristic of schwertmannite (Bigham and Nordstrom, 2000), an iron-oxide phase that is stable under acid conditions (Majzlan *et al.*, 2004). The precipitation of schwertmannite apparently reflects local exhaustion of carbonate and, consequently, depletion of the buffer capacity of the rock. Solution pH should decline as iron oxide precipitates, thus stabilizing schwertmannite. Although schwertmannite is associated typically with acid rock drainage, it is stable relative to ferrihydrite "over a wide range of pH when the system contains even a small amount of sulfate" (Majzlan *et al.*, 2004).

Life thrives by exploiting systems that are out of equilibrium to obtain the energy necessary for catabolic and anabolic processes. Although most interpretations of patterned rocks do not explicitly consider the possibility that life was involved in the generation of the pattern (*e.g.*, Singer and Navrot, 1970; Hintze, 1986; Fu *et al.*, 1994; Frankie and Jacobson, 2001; Marko *et al.*, 2003; McBride, 2003; Pickett, 2003; Wells *et al.*, 2003; Serra *et al.*, 2010; Jamtveit *et al.*, 2011), biological systems (*e.g.*, bacteria, Lacasta *et al.*, 1999; concentric demyelination in the human brain, Khonsari and Calvez, 2007) are known to generate patterns that have similarities to Liesegang. How does the formation of the thick bands of microbially oxidized IOC differ from the formation of Liesegang bands? Each band of IOC began precipitation at a steep gradient in oxygen/aqueous Fe^{2+}. This gradient was apparently stabilized by microbial activity. Each band of IOC represents a distinct iron-oxide precipitation event. Precipitation began when microbes began to exploit the gradient and ended when life could no longer preserve that gradient in space. The true Liesegang process, on the other hand, requires that solutes diffuse freely through the region where multiple bands of iron oxide may be precipitating simultaneously. It seems unlikely, therefore, that microbes would generate thick *Liesegang* bands of IOC.

Our interpretation of the Shinarump wonderstone is that the sandstone was cemented locally with siderite during early methanic diagenesis (Fig. 15). The sandstone was fractured by joints during Basin and Range tectonism and infiltrated by oxygenated groundwaters during uplift of the Colorado Plateau. Iron-oxidizing bacteria colonized the redox interface between the oxidizing groundwaters and siderite cement. The microbes oxidized aqueous Fe^{2+} that diffused to the stabilized redox interface. The IOS marks reaction finger fronts (Ortoleva, 1994) produced as acid diffused away from newly precipitated ferric oxyhydroxide toward the reduced, siderite-cemented sandstone (Fig. 15). Each band of IOC represents a stabilized redox interface between the oxidizing portion of the aquifer and the more
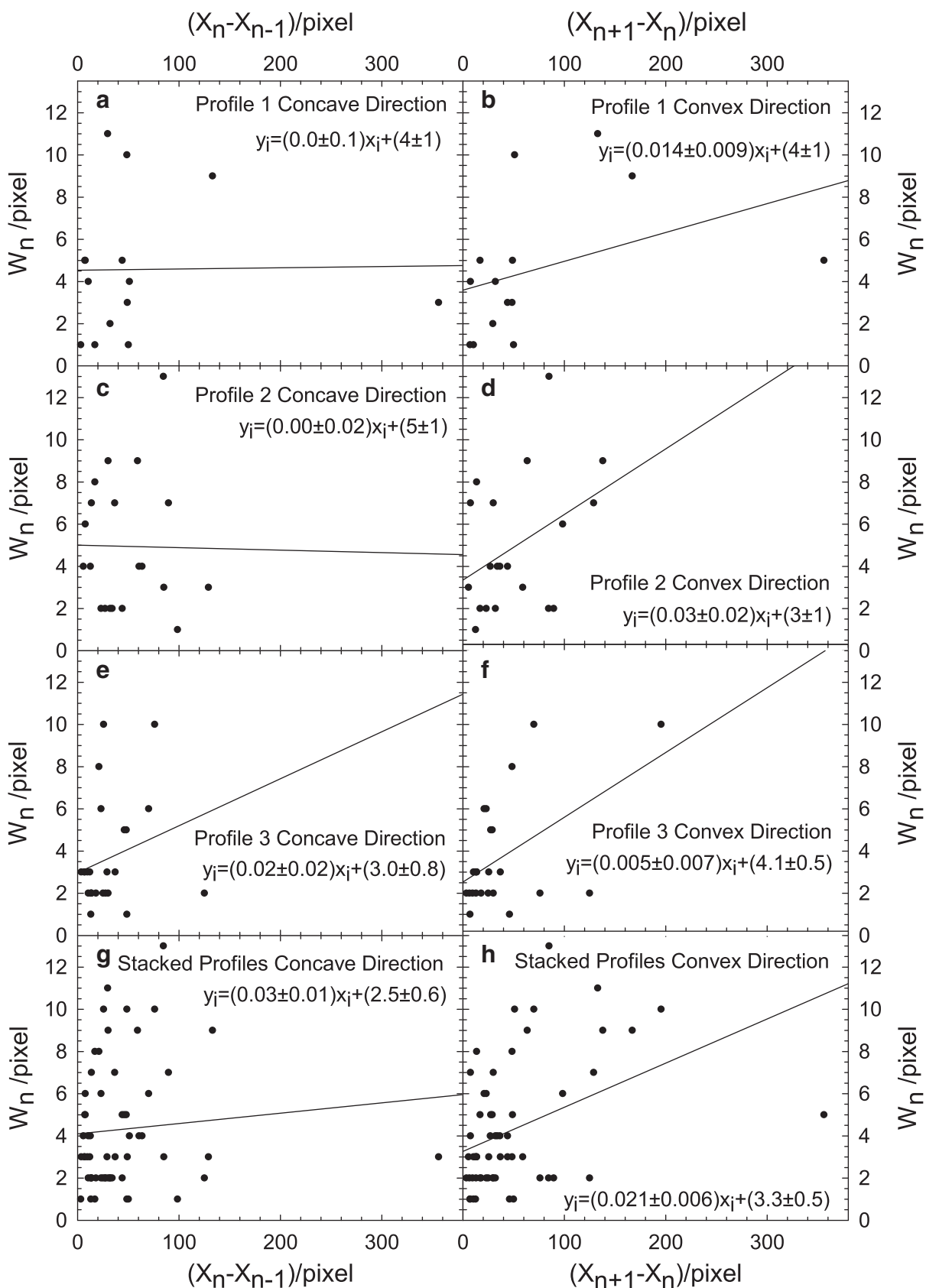
FIG. 13. (**a–f**) Test of band thickness against distance between bands measured in the concave (graphs on left-hand side) and convex (graphs on right-hand side) direction for Profiles 1–3 on Image P3180044 (Fig. 3) and (**g–h**) the combined results for all three profiles.
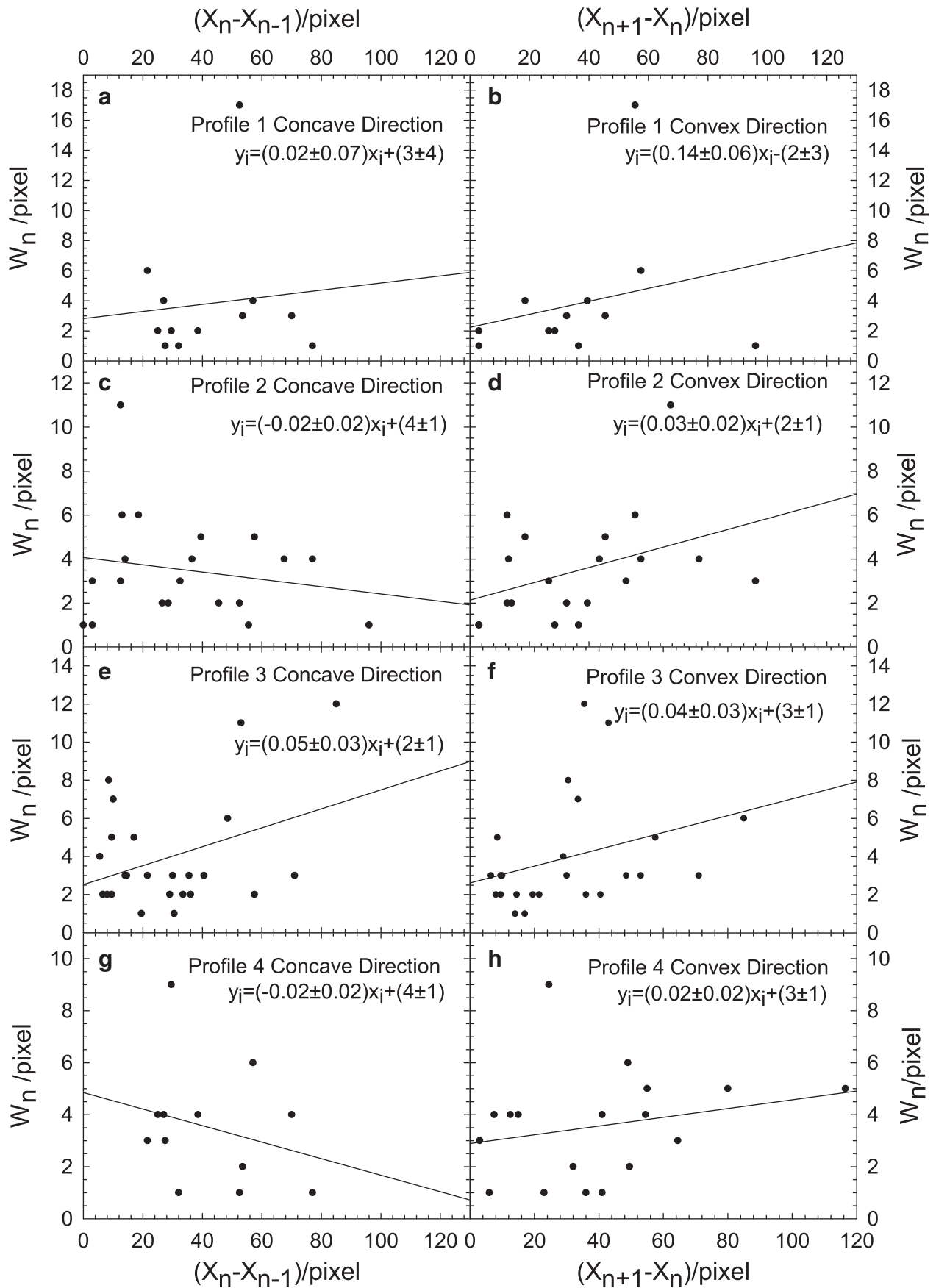
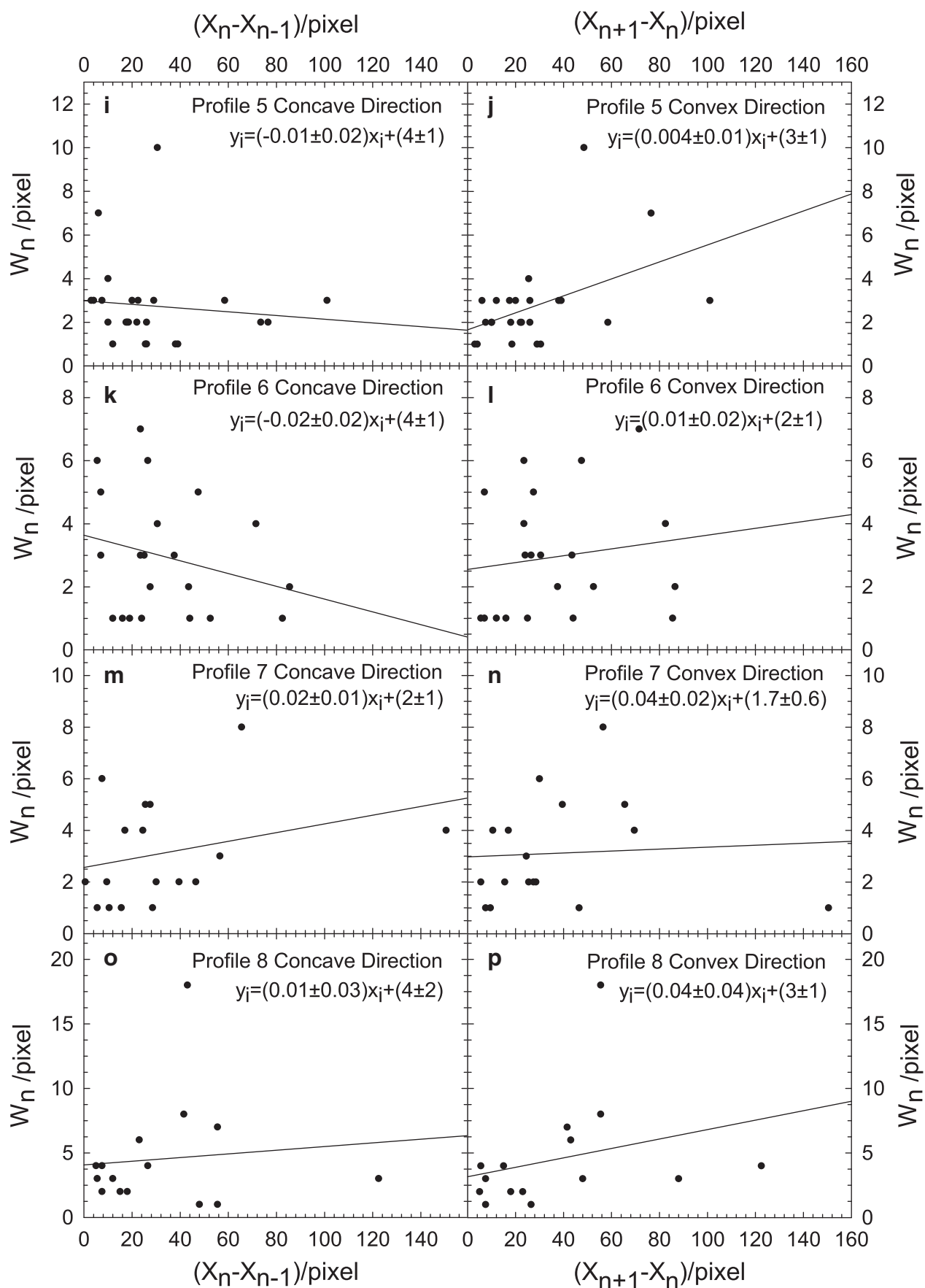**FIG. 14.**   Panels **a–h** (*continued next page*).

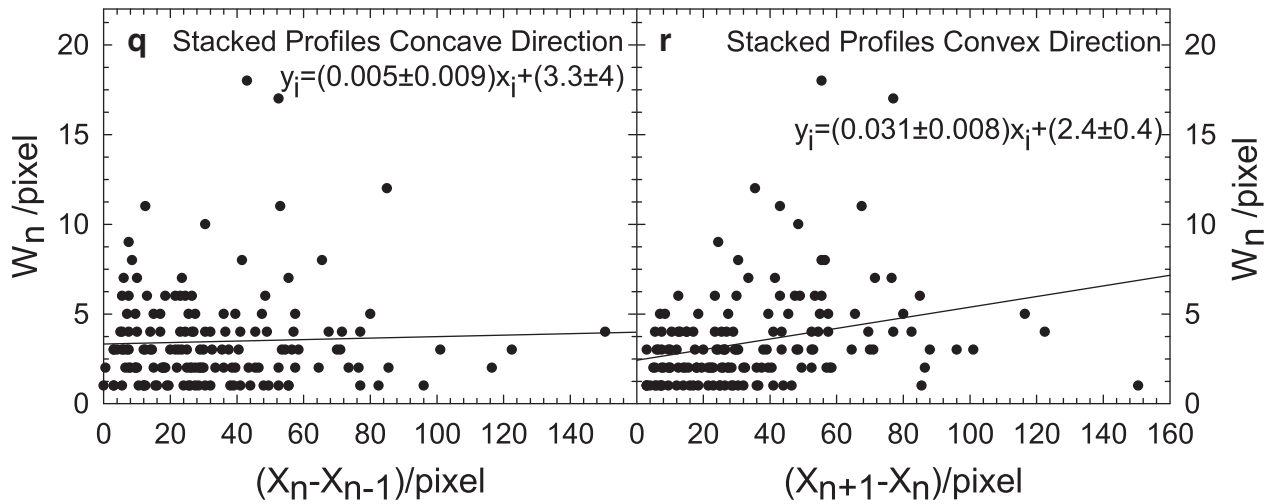**FIG. 14.** Panels **i–p** (*continued next page*).

FIG. 14. (**a**–**p**) Test of band thickness against distance between bands measured in the concave (graphs on left-hand side) and convex (graphs on right-hand side) direction for Profiles 1–8 on Image P3190192 (Fig. 4) and (**q**–**r**) the combined results for all eight profiles.

reduced, siderite-bearing portion of the system. Eventually, each stabilized interface in turn became unstable. It is possible that the microbial system lost the capacity to occlude oxidizing waters, or the iron-oxidation reactions might have become less exergonic with local depletion of Fe^{2+} as the siderite front became more distant, or the accumulation of acid may have driven local pH values below the range in which iron-oxidizing bacteria could thrive. In any event, a new interface was established and colonized by microbes. Finally, the geometry of the interface was such that microbes were able to completely isolate a volume of rock (Fig. 15m–15n) until all the reduced iron within had been oxidized.

We interpret the IOS to have been produced during the breakthrough of oxygenated waters as the redox interface advanced within the rock. The interaction between residual Fe^{2+} absorbed on sand grains and invading oxygenated waters would mimic the geometry of the Liesegang phenomenon. In this interpretation (and in the absence of evidence for microbial activity in the precipitation of the IOS), the IOS is the product of apparently abiotic oxidation of Fe^{2+} that remains between a band of IOC and the siderite-cemented sandstone. Bleaching of IOS (Figs. 1 and 15) must occur after the IOS is formed and may be the product of iron-reducing bacteria obtaining electrons from the carbon fixed by the iron oxidizers.

6. Conclusions

The iron-oxide cementation and staining produced by the wonderstone phenomenon comprises a microbially induced structure (*cf.* MISS of Noffke, 2009). The presence of apparent local rhombohedral pseudomorphs of siderite is evidence that a reduced iron phase was present in the rock prior to infiltration by oxidizing groundwaters. Relationships between the width of IOC bands and interband distance are best explained by dissolution of siderite ($FeCO_3$) with subsequent oxidation and accu-

mulation of iron at a series of redox interfaces. The bands of IOC contain abundant iron-oxide-encrusted stalks similar in size and morphology to modern *Gallionella* spp. Although the spacing of bands of IOC is incompatible with typical examples of the Liesegang phenomenon, the spacing and width of IOS *between* bands of IOC *are* fully consistent with true Liesegang. The wonderstone pattern is, therefore, a microbially induced structure comprising microbially mediated iron-oxide cementation and apparently abiotic Liesegang.

These distinctive patterns have exobiological significance for five reasons, as follows: (1) Because reduced carbon is unstable in the presence of excess Fe(III), it has been argued that ferric oxide–bearing rocks are a poor choice for exobiological exploration (*e.g.*, Sumner, 2004). The results obtained here are evidence that oxidized iron need not be considered a risk when exploring for life on other planets. On the contrary, if interpreted properly, patterns of iron-oxide mineralization could be used to guide selection of samples for analysis on site, as well as for sample return missions. (2) The patterns are megascopic evidence of subsurface microbial activity. Many of the wonderstone and so-called Liesegang features observed in the Shinarump and in other formations can be measured in meters. (3) Because rock cemented by iron oxide is more resistant to weathering and erosion than unconsolidated sediment, these features may be relatively easy to observe using remote methods. (4) The evidence that siderite formed on Mars is compelling (Niles *et al.*, 2013; Tomkinson *et al.*, 2013), and siderite would be expected to be the product of the interaction of carbon dioxide–charged fluids and iron-rich rocks (Niles *et al.*, 2013). (5) Although siderite provides an optimal microbial substrate in that it combines a carbon source and electron donor, iron-oxidizing bacteria are known to thrive on other ferrous iron minerals (Emerson *et al.*, 2010). These features may, therefore, occur in a wide variety of rock types.
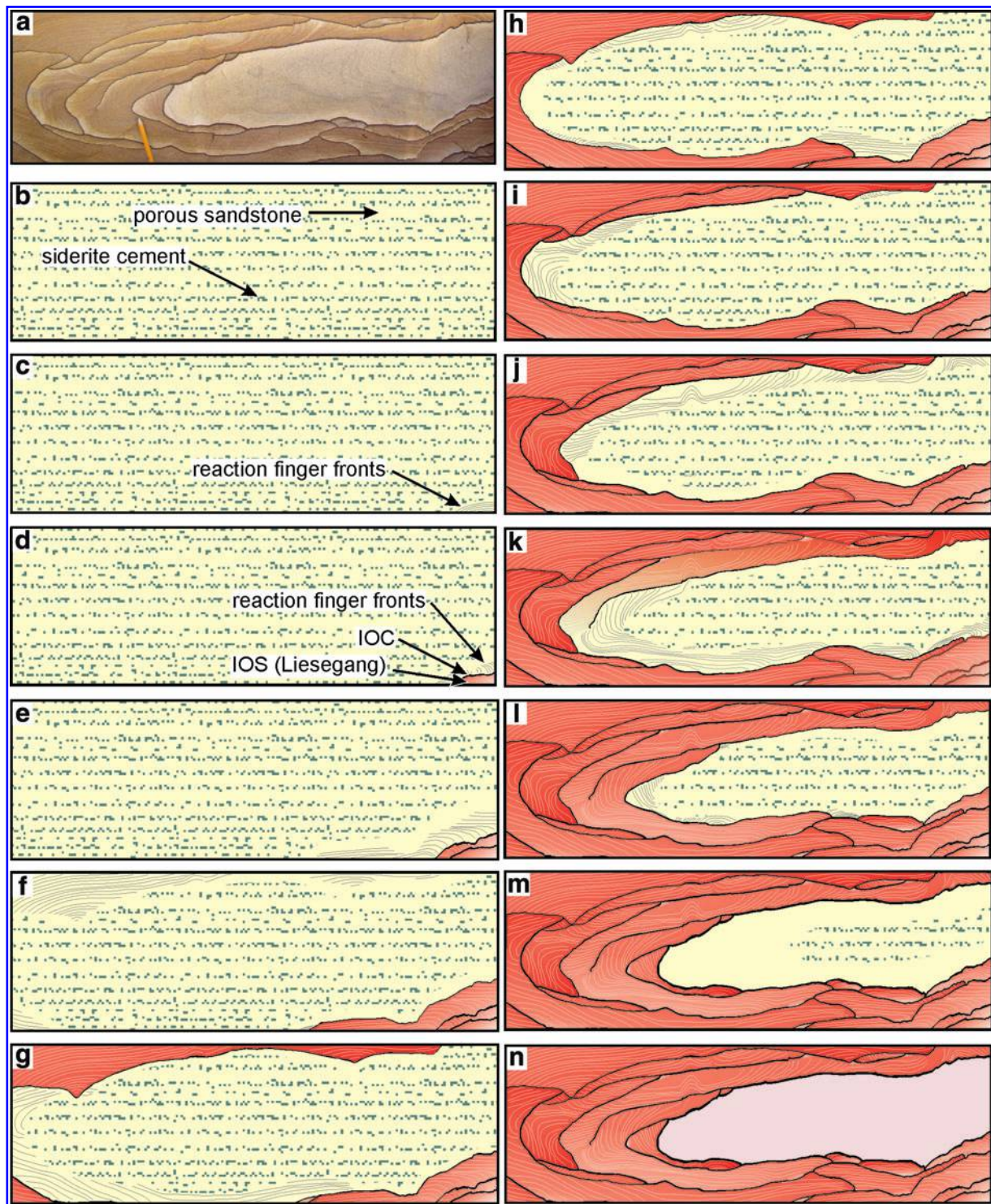
FIG. 15. Image of wonderstone and a sequence of diagrams that illustrate development of the wonderstone pattern. Initial porous sandstone (yellow) is cemented locally by siderite [green in (b–m)]. IOC forms out of field of view in (c) from iron obtained by dissolution of siderite in lower right-hand corner. Arcuate lines in (c) represent reaction finger fronts (*sensu* Ortoleva, 1994). After abiotic oxidation of residual iron material in lower right corner to produce iron-oxide-stained rock (shades of red), another redox interface is established, and IOC (black) begins to accumulate in (d). The iron in this band of IOC was derived from the cement dissolved in the area above and to the left of the band of IOC. Panels (e–l) illustrate the continuing development of the bands of IOC and IOS. Panels (m–n) illustrate the isolation and complete bleaching of the iron in the interior of the diagram as the last band of IOC formed. (Color graphics available at www.liebertonline.com/ast)

Acknowledgments

We thank Dr. H. Chen for assistance with electron microscopy and Mr. Kenneth Brown for samples and field access. Support for this research was provided by the NASA Nebraska Space Grant program and the UNL Vice-Chancellor for Research. Paul Niles acknowledges support from the NASA Johnson Space Center and the Mars Fundamental Research Program. Conversations in the field with P. Reiners and B. Toro have improved our interpretation. Reviews of multiple versions of this manuscript by five anonymous reviewers have helped to improve the final product.

Author Disclosure Statement

The authors declare that they have no commercial associations that might create a conflict of interest in connection with this manuscript.

References

Al-Ghoul, M., Ammar, M., and Al-Kaysi, R.O. (2012) Band propagation, scaling laws and phase transition in a precipitate system. I: Experimental study. *J Phys Chem A* 116:4427–4437.

Allen, C.C., Westall, F., and Schelble, R.T. (2001) Importance of a martian hematite site for astrobiology. *Astrobiology* 1:111–123.

Antal, T., Droz, M., Mangin, J., Rácz, Z., and Zrinyi, M. (1998) Derivation of the Matalon-Packter law for Liesegang patterns. *J Chem Phys* 109:9479–9486.

Berner, R.A. (1981) A new geochemical classification of sedimentary environments. *Journal of Sedimentary Research* 51:359–365.

Bigham, J.M. and Nordstrom, D.K. (2000) Iron and aluminum hydroxysulfates from acid sulfate waters. In *Sulfate Minerals: Crystallography, Geochemistry, and Environmental Significance*, Reviews in Mineralogy and Geochemistry Vol. 40, edited by C.N. Alpers, J.L. Jambor, and D.K. Nordstrom, Mineralogical Society of America, Washington, DC, pp 351–403.

Billingsley, G.H., Priest, S.S., and Felger, T.J. (2004) *Geologic Map of Pipe Spring National Monument and the Western Kaibab-Paiute Indian Reservation, Mohave County, Arizona*, Scientific Investigations Map 2863, U.S. Geological Survey, Reston, VA. Available online at http://pubs.usgs.gov/sim/2004/2863

Billingsley, G.H., Priest, S.S., and Felger, T.J. (2008) *Geologic Map of the Fredonia 30′×60′ Quadrangle, Mohave and Coconino Counties, Northern Arizona*, Scientific Investigations Map 3035, U.S. Geological Survey, Reston, VA. Available online at http://pubs.usgs.gov/sim/3035

Chan, C.S., De Stasio, G., Welch, S.A., Girasole, M., Frazier, B.H., Nesterova, M.V., Fakra, S., and Banfield, J.F. (2004) Microbial polysaccharides template assembly of nanocrystal fibers. *Science* 303:1656–1658.

Chan, M.A., Potter, S.L., Bowen, B.B., Parry, W.T., Barge, L.M., Seiler, W., Peterson, E.U., and Bowman, J.R. (2012) Characteristics of terrestrial ferric oxide concretions and implications for Mars. In *Sedimentary Geology of Mars*, SEPM Special Publication 102, edited by J.R. Grotzinger and R.E. Milliken, Society for Sedimentary Geology, Tulsa, OK, pp 253–270.

Dickinson, W.R., Gehrels, G.E., and Stern, R.J. (2010) Late Triassic Texas uplift preceding Jurassic opening of the Gulf of Mexico: evidence from U-Pb ages of detrital zircons. *Geosphere* 6:641–662.

Doelling, H.H. and Davis, F.D. (1989) *The Geology of Kane County, Utah*, Utah Geological and Mineral Survey Bulletin 124, Utah Geological and Mineral Survey, Salt Lake City, UT.

Draper, N.R. and Smith, H. (1966) *Applied Regression Analysis*, John Wiley & Sons, New York.

Emerson, D. and Revsbech, N.P. (1994) Investigation of an iron-oxidizing microbial mat community located near Aarhus, Denmark: field studies. *Appl Environ Microbiol* 60:4022–4031.

Emerson, D., Fleming, E.J., and McBeth, J.M. (2010) Iron-oxidizing bacteria: an environmental and genomic perspective. *Annu Rev Microbiol* 64:561–583.

Evensen, C.G. (1958) The Shinarump Member of the Chinle Formation. In *Guidebook of the Black Mesa Basin, Northeastern Arizona. New Mexico Geological Society Ninth Field Conference*, edited by R.Y. Anderson and J.W. Harshberger, New Mexico Geological Society, Socorro, NM, pp 95–97.

Feeney, R., Schmidt, S.L., Strickholm, P., Chadam, J., and Ortoleva, P. (1983) Periodic precipitation and coarsening waves: application of the competitive particle growth model. *J Chem Phys* 78:1293–1311.

Fleming, E.J., Cetinic, I., Chan, C.S., Whitney King, D., and Emerson, D. (2014) Ecological succession among iron-oxidizing bacteria. *ISME J* 8:804–815.

Frankie, W.T. and Jacobson, R.J. (2001) *Guide to the Geology of the Garden of the Gods Area, Gallatin, Hardin, Pope, and Saline Counties, Illinois*, Illinois State Geological Survey Field Trip Guidebook 2001A,B, Illinois State Geological Survey, Champaign, IL.

Fu, L., Milliken, K.L., and Sharp, J.M., Jr. (1994) Porosity and permeability variations in fractured and Liesegang-banded Breathitt sandstones (Middle Pennsylvanian), eastern Kentucky: diagenetic controls and implications for modeling dual porosity systems. *J Hydrol* 154:351–381.

Hallberg, R. and Ferris, G. (2004) Biomineralization by *Gallionella*. *Geomicrobiol J* 21:325–330.

Harwood, J.W., Aplin, A.C., Fialips, C.I., Illiffe, J.E., Kozdon, R., Ushikubo, T., and Valley, J.W. (2013) Quartz cementation history of sandstones revealed by high resolution SIMS oxygen isotope analysis. *Journal of Sedimentary Research* 83:522–530.

Hemphill W.R. (1956) *Photogeologic Map of the Fredonia NW Quadrangle Mohave County, Arizona*, Miscellaneous Geologic Investigations Map I-133, U.S. Geological Survey, Reston, VA. Available online at http://ngmdb.usgs.gov/Prodesc/proddesc_1513.htm

Henisch, H.K. (1988) *Crystals in Gels and Liesegang Rings: In Vitro Veritas*, Cambridge University Press, Cambridge, UK.

Hintze, L.F. (1986) Stratigraphy and structure of the Beaver Dam Mountains, southwestern Utah. In *Thrusting and Extensional Structures and Mineralization in the Beaver Dam Mountains, Southwestern Utah*, Utah Geological Association Publication 15, edited by D.T. Griffen and W.R. Phillips, Utah Geological Association, Salt Lake City, UT, pp 1–36.

Hofmann, B.A. and Farmer, J.D. (2000) Filamentous fabrics in low-temperature mineral assemblages: are they fossil biomarkers? Implications for the search for a subsurface fossil record on the early Earth and Mars. *Planet Space Sci* 48:1077–1086.

Hunt, P.A., Mitchell, P.B., and Paton, T.R. (1977) "Laterite profiles" and "lateritic ironstones" on the Hawkesbury Sandstone, Australia. *Geoderma* 19:105–121.

Jablczynski, K. (1923) La formation rhythmique des précipités: les anneaux de Liesegang. *Bulletin de la Société Chimique de France* 33:1592–1597.

Jamtveit, B. and Hammer, Ø. (2012) Sculpting of rocks by reactive fluids. *Geochemical Perspectives* 1:341–481.

Jamtveit, B., Kobchenko, M., Austrheim, H., Malthe-Sørenssen, A., Røyne, A., and Svensen, H. (2011) Porosity evolution and crystallization-driven fragmentation during weathering of andesite. *J Geophys Res* 116, doi:10.1029/2011JB008649.

Karam, T., El-Rassy, H., and Sultan, R. (2011) Mechanism of revert spacing in a $PbCrO_4$ Liesegang system. *J Phys Chem A* 115:2994–2998.

Kettler, R.M., Loope, D.B., and Weber, K.A. (2010) Geological evidence of microbial dissolution of iron carbonate. *Geochim Cosmochim Acta* 74(Suppl. 1):A509.

Khonsari, R.H. and Calvez, V. (2007) The origins of concentric demyelination: self-organization in the human brain. *PLoS One* 2, doi:10.1371/journal.pone.0000150.

Kim, J., Kim, S., and Tazaki, K. (2002) Mineralogical characterization of microbial ferrihydrite and schwertmannite, and non-biogenic Al-sulfate precipitates from acid mine drainage in the Donghae mine area, Korea. *Environ Geol* 42:19–31.

Krepski, S.T., Emerson, D., Hredzak-Showalter, P.L., Luther, G.W., III, and Chan, C.S. (2013) Morphology of biogenic iron oxides records microbial physiology and environmental conditions: toward interpreting iron microfossils. *Geobiology* 11:457–471.

Lacasta, A.M., Cantalapiedra, I.R., Auguet, C.E., Peñaranda, A., and Ramírez-Piscina, L. (1999) Modelling of spatiotemporal patterns in bacterial colonies. *Phys Rev E Stat Nonlin Soft Matter Phys* 59:7036–7041.

Lai, Y., Chen, C., and Tang, H. (2012) Paleoproterozoic positive $\delta^{13}C$ excursion in Henan, China. *Geomicrobiol J* 29:287–298.

L'Heureux, I. (2013) Self-organized rhythmic patterns in geochemical systems. *Philos Trans A Math Phys Eng Sci* 371, doi:10.1098/rsta.2012.0356.

Liesegang, R.E. (1896) Ueber einige Eigenschaften von Gallerten. *Naturwissenschaftliche Wochenschrift* 11:353–362.

Loope, D.B., Kettler, R.M., and Weber, K.A. (2010) Follow the water: connecting a CO_2 reservoir and bleached sandstone to iron-rich concretions in the Navajo Sandstone of south-central Utah, USA. *Geology* 38:999–1002.

Loope, D.B., Kettler, R.M., and Weber, K.A. (2011) Morphologic clues to the origins of iron oxide–cemented spheroids, boxworks, and pipelike concretions, Navajo Sandstone of south-central Utah, U.S.A. *J Geol* 119:505–520.

Loope, D.B., Kettler, R.M., Weber, K.A., Hinrichs, N.L., and Burgess, D.T. (2012) Rinded iron-oxide concretions: hallmarks of altered siderite masses of both early and late diagenetic origin. *Sedimentology* 59:1769–1781.

Majzlan, J., Navrotsky, A., and Schwertmann, U. (2004) Thermodynamics of iron oxides: part III. Enthalpies of formation and stability of ferrihydrite ($\sim Fe(OH)_3$), schwertmannite ($\sim FeO(OH)_{3/4}(SO_4)_{1/8}$), and ε-Fe_2O_3. *Geochim Cosmochim Acta* 68:1049–1059.

Marko, F., Pivko, D., and Hurai, V. (2003) Ruin marble: a record of fracture-controlled fluid flow and precipitation. *Geological Quarterly* 47:241–252.

McBride, E.F. (2003) Pseudofaults resulting from compartmentalized Liesegang bands: update. *Sedimentology* 50:725–730.

Morris, R.H. (1957) *Photogeologic Map of the Fredonia NE Quadrangle Mohave County, Arizona*, Miscellaneous Geologic Investigations Map I-247, U.S. Geological Survey, Reston, VA. Available online at http://ngmdb.usgs.gov/Prodesc/proddesc_1512.htm

Niles, P.B., Catling, D.C., Berger, G., Chassefière, E., Ehlmann, B.L., Michalski, J.R., Morris, R., Ruff, S.W., and Sutter, B. (2013) Geochemistry of carbonates on Mars: implications for climate history and nature of aqueous environments. *Space Sci Rev* 174:301–328.

Noffke, N. (2009) The criteria for the biogeneicity of microbially induced sedimentary structures (MISS) in Archean and younger, sandy deposits. *Earth-Science Reviews* 96:173–180.

Ortoleva, P. (1984) The self-organization of Liesegang bands and other precipitate patterns. In *Chemical Instabilities*, edited by G. Nicolis and F. Baras, D. Reidel Publishing Company, Dordrecht, the Netherlands, pp 289–297.

Ortoleva, P. (1994) *Geochemical Self-Organization*, Oxford University Press, New York.

Ortoleva, P., Merino, E., Moore, C., and Chadam, J. (1987) Geochemical self-organization I: reaction-transport feedbacks and modeling approach. *Am J Sci* 287:979–1007.

Pickett, J.W. (2003) Stratigraphic relationships of laterite at Little Bay, near Maroubra, New South Wales. *Australian Journal of Earth Sciences* 50:63–68.

Reiners, P.W., Chan, M.A., and Evenson, N.S. (2014) (U-Th)/He geochronology and chemical compositions of diagenetic cement, concretions, and fracture-filling oxide minerals in Mesozoic sandstones of the Colorado Plateau. *Geol Soc Am Bull* 126:1363–1383.

Ridgway, H.F., Means, E.G., and Olson, B.H. (1981) Iron bacteria in drinking-water distribution systems: elemental analysis of *Gallionella* stalks, using X-ray energy-dispersive microanalysis. *Appl Environ Microbiol* 41:288–297.

Robinson, E.A. (1985) Fundamentals of seismic exploration. In *Maximum-Entropy and Bayesian Methods in Inverse Problems*, edited by C.R. Smith and W. Grandy Jr., D. Reidel Publishing Company, Dordrecht, the Netherlands, pp 171–210.

Sable, E.G. and Hereford, R. (2004) *Geologic Map of the Kanab 30′×60′ Quadrangle, Utah and Arizona*, Geologic Investigations Series I-2655, U.S. Geological Survey, Reston, VA. Available online at http://pubs.usgs.gov/imap/2655

Schneider, C.A., Rasband, W.S., and Eliceri, K.W. (2012) NIH Image to ImageJ: 25 years of image analysis. *Nat Methods* 9:671–675.

Seilacher, A. (2001) Concretion morphologies reflecting diagenetic and epigenetic pathways. *Sediment Geol* 143:41–57.

Serra, M., Borghi, A., Gallo, L.M., Hovoric, R., and Vaggelli, G. (2010) Petrographic features, genesis and provenance of Pietra Paesina collections of the Regional Museum of Natural Sciences of Turin, Italy. *Periodico di Mineralogia* Special Issue, 95–111, doi:10.2451/2010PM0024.

Singer, A. and Navrot, J. (1970) Diffusion rings in altered basalt. *Chem Geol* 6:31–41.

Sumner, D.Y. (2004) Poor preservation potential of organics in Meridiani Planum hematite-bearing sedimentary rocks. *J Geophys Res* 109, doi:10.1029/2004JE002321.

Suzuki, T., Hashimoto, H., Matsumoto, N., Furutani, M., Kunoh, H., and Takada, J. (2011) Nanometer-scale visualization and structural analysis of the inorganic/organic hybrid

structure of *Gallionella ferruginea* twisted stalks. *Appl Environ Microbiol* 77:2877–2881.

Tomkinson, T., Lee, M.R., Mark, D.F., and Smith, C.L. (2013) Sequestration of Martian CO_2 by mineral carbonation. *Nat Commun* 4, doi:10.1038/ncomms3662.

Vasconcelos, P.M., Heim, J.A., Farley, K.A., Monteiro, H., and Waltenberg, K. (2013) $^{40}Ar/^{39}Ar$ and (U–Th)/He–$^4He/^3He$ geochronology of landscape evolution and channel iron deposit genesis at Lynn Peak, Western Australia. *Geochim Cosmochim Acta* 117:283–312.

Weber, K.A., Spanbauer, T.L., Wacey, D., Kilburn, M.R., Loope, D.B., and Kettler, R.M. (2012) Biosignatures link microorganisms to iron mineralization in a paleoaquifer. *Geology* 40:747–750.

Wells, N.A., Waugh, D.A., and Foos, A.M. (2003) Some notes and hypotheses concerning iron and iron remobilization features in the Sharon Formation (Summit County, Ohio). In *Pennsylvanian Sharon Formation Past and Present: Sedimentology, Hydrogeology, and Historical and Environmental Significance*, Guidebook No. 18, edited by A.M. Foos, Ohio Department of Natural Resources, Columbus, OH, pp 33–47.

Address correspondence to:
Richard M. Kettler
Department of Earth and Atmospheric Sciences
University of Nebraska-Lincoln
Lincoln NE 68588-0340

E-mail: rkettler1@unl.edu

Abbreviations Used

ANOVA = analysis of variance
DoF = degrees of freedom
IOC = iron-oxide cement
IOS = iron-oxide stain
MISS = microbially induced sedimentary structures
MS = mean square
SEM = scanning electron microscope
SS = sum of squares